



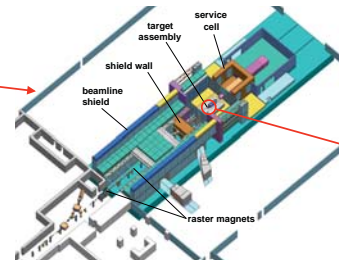
Irradiation environment in the proposed Materials Test Station

E. Pitcher, LANSCE-DO

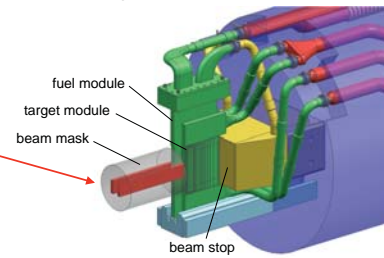
Los Alamos Neutron Science Center



"Area A" Experimental Hall at LANSCE



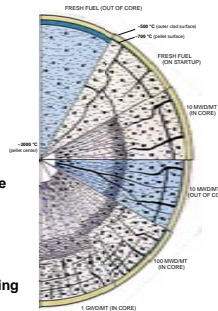
MTS Target Assembly



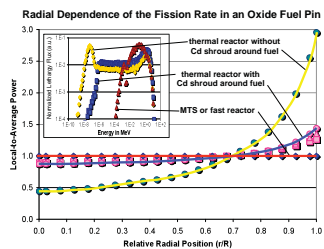
The MTS will be built in an existing experimental hall at the Los Alamos Neutron Science Center (LANSCE). It will be unique among nuclear fuel irradiation facilities in that the source of neutrons used to irradiate samples is nuclear spallation rather than fission. The facility is driven by a high-power proton beam, which produces neutrons through nuclear interactions with tungsten nuclei. About 16 neutrons are produced for every proton incident on the tungsten target. A 1-MW proton beam can generate a fast neutron flux that approaches the flux produced by the world's most powerful research fast reactors. Once built, the MTS will be the *only* fast spectrum irradiation facility operating outside the Asian continent.

Evolution of oxide fuel in a fast reactor: Behavior that MTS will replicate

- Pellet cracking caused by large thermal stresses in ceramic fuel
- Central void formation from high fuel centerline temperature
- Phase changes / recrystallization
- Changes in stoichiometry (oxygen/metal ratio)
- Thermal-gradient-induced actinide and fission product transport
- Fuel-clad interactions
 - mechanical
 - chemical
- Radiation-induced aging of cladding



MTS does not produce a "rim effect," as do shielded irradiations in a thermal reactor

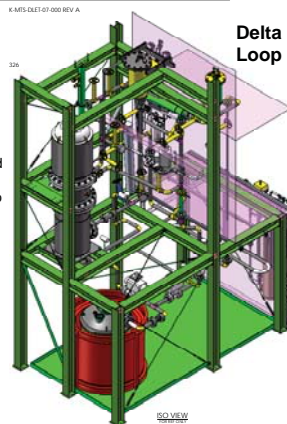


H.J. MacLean & S.L. Hayes, "Irradiation Testing for AFCL," July 21, 2009.

- As in a fast reactor, the lack of thermal neutrons in MTS yields a uniform fission rate throughout the fuel pellet
- Shielded irradiations in a thermal reactor exhibit a small "rim effect" yielding
 - A non-prototypic fuel centerline temperature (lower by at least 60°C)
 - Non-prototypic temperature gradient, affecting fission product transport and stoichiometry
- Rim effect worsens as thermal shield burns up

Lead-Bismuth Eutectic Coolant Research Using LANL's Delta Loop

To accommodate the high heat flux and high operating temperature of the nuclear test fuel, the MTS uses lead-bismuth eutectic (LBE) to cool the fuel and the spallation target. LANL has extensive experience with LBE, having constructed the Delta Loop in 2000 and operated it until 2008. During Preliminary Design, the MTS project plans to conduct a number of experiments on the loop to confirm design elements, such as a fast-response heat exchanger, corrosion tests, and pressure drops in loop components.

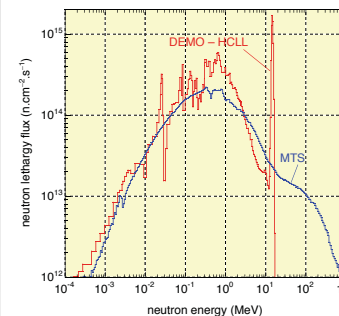
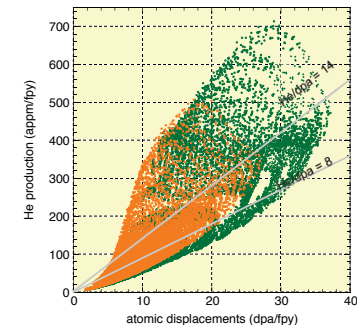


A number of next-generation fast-spectrum nuclear reactors that use lead-alloy coolant have been proposed. The Delta Loop can be used to conduct supporting research on lead alloy coolant performance, addressing such questions as:

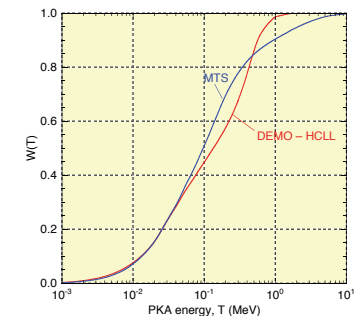
- Erosion tests at >2 m/s fluid velocity as a $f(T, O_2)$
- Long-term (>12,000 h) corrosion as a $f(\text{alloy}, T, O_2)$
- Liquid metal embrittlement studies
- Thermal hydraulic tests (flow rate, pressure drop) of specific SMR geometries
- Instrumentation development and testing (oxygen concentration, flow rate, velocity profiles, corrosion rate)
- Techniques for oxygen control in SMR application
- LBE purification and conditioning

Fusion Materials Irradiation Conditions

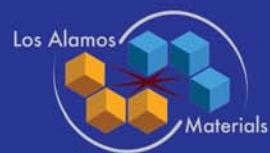
At a beam power of 1 MW, the range of displacement and He production rates in iron accessible in the MTS irradiation regions is shown in the figure at right. Each pixel plotted represents a 40-mm³ volume element in either the fuel (green pixels) or material (orange pixels) irradiation regions. A broad range of He-to-dpa ratios are available, from 5 to 33 appm/dpa, which will allow scientists to measure materials properties as a function of this important parameter. Shown below are the neutron spectra and damage production functions $W(T)$ for the MTS and the Helium-Cooled Lithium Lead (HCLL) blanket of the proposed DEMO reactor. Good agreement of $W(T)$ is seen for the two facilities for $T < 50$ keV. For DEMO, nearly all displacements are caused by PKA's with energies less than 1 MeV. For the MTS, PKA's with $T > 1$ MeV (0.4% of all PKA's) are responsible for nearly 10% of all atomic displacements.



Neutron Spectrum



Damage Production Function



LANSCCE: Nuclear physics and material science

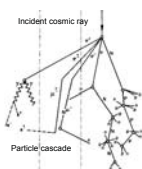
J. Ullmann, LANSCE-NS



- The Los Alamos Neutron Science Center (LANSCCE) has an active program in basic and applied nuclear physics
- Some research directly related to materials properties – “single-event” effects in electronics
- Research on nuclear reactions that produce hydrogen and helium that can lead to embrittlement of metals
- Production of radioisotopes for the national and international user communities.

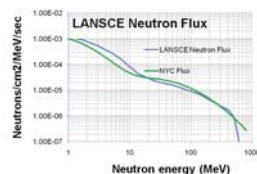
Accelerated Testing Of Electronics

S.A. Wender (LANSCCE-NS) Principal Investigator



- Failures in electronic components due to nuclear reactions caused by cosmic-ray neutrons
- Neutrons produced from cascades caused by high-energy cosmic rays interacting in the atmosphere

- LANSCE/WNR neutron flux similar in energy dependence to atmospheric cosmic-ray induced neutron flux, but 10^7 times more intense

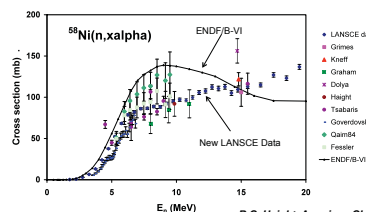


- Major electronic component manufacturers and users, including aircraft and computer manufacturers, test components at LANSCE to certify failure rate.
- 80% of the LANL “Q-machine” computer failures were found to be due to neutron-induced effects by testing a module at LANSCE. IEEE Trans. Dev. Mat. Reliab. 5, 2005).
- Failures traced to cache memory that was not error corrected.

Gas Production in Structural Elements

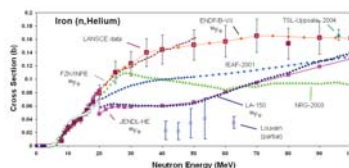
R.C. Haight (LANSCCE-NS) Principal Investigator

- Gas production (He and H) by neutrons on structural and other materials (Fe, Cr, Ni, Zr, Ta, W, etc) is important for understanding radiation effects.
- High-temperature helium embrittlement could be a one factor that limits lifetime of components in (possible) fusion power reactors.
- Fission-power reactor lifetime extension may also require careful evaluation of neutron-induced embrittlement.
- New measurements of neutron-induced helium production cross sections made at LANSCE/WNR differ considerably from the ENDF/B-VI evaluated values used in Monte Carlo calculations using the MCNP program.



Comparison of new LANSCE/WNR data for $^{58}\text{Ni}(n,\alpha)$ compared to previous measurements and the ENDF/B-VI evaluation.

R.C. Haight, American Chemical Society, New Orleans LA, April 19, 2008. (LAUR-08-2160)



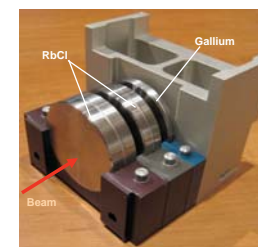
Comparison of new LANSCE/WNR data for $^{56}\text{Fe}(n,\alpha)$ compared to previous measurements and several evaluations, including the new ENDF/B-VII results.

R.C. Haight, and T.S. Hill, 16th Pacific Basin Nuclear Conference, Aomori, Japan, Oct 13-18, 2008.

Radioisotope Production at LANSCE

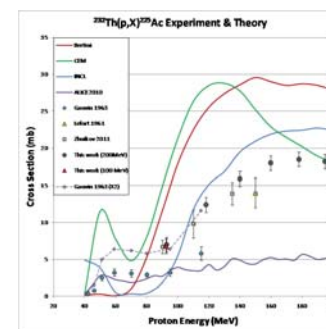
F.M. Nortier, Principal Investigator

- Isotopes produced with 100 MeV, 250 μA proton beam at Isotope Production Facility
- 95% of beam time devoted to production of ^{82}Sr and ^{68}Ge
- ^{82}Sr ($T_{1/2} = 22.5$ days) is source of ^{82}Rb ($T_{1/2} = 75$ sec) used in positron emission tomography (PET) for myocardial perfusion imaging
 - LANSCE produces enough for 20,000 cardiac studies per month
- ^{68}Ge ($T_{1/2} = 270.8$ days) is used for PET scan calibration
 - LANSCE produces >50% of world's supply
- Radioisotopes produced by irradiation of ^{nat}Rb and ^{nat}Ga followed by radiochemical separation
- Other isotopes produced include ^{22}Na and ^{88}Y



IPF Target Assembly

- Rb targets consist of $^{nat}\text{RbCl}$ salt cast in a “hockey puck” and contained in 5 cm, dia Inconel containers with 0.3 mm window
- Ga target is ^{nat}Ga metal in Nb capsule
- Both target assemblies have experienced occasional premature failures during irradiation. These failures are not well understood



Recent LANSCE/IPF measurements of ^{225}Ac production from ^{232}Th compared to previous data and calculations using various models. Black circles used the 200 MeV beam, red triangle used 100 MeV beam at IPF.

- Programs to develop methods for making new radioisotopes
- Example: ^{225}Ac
- $T_{1/2} = 10$ d followed by 4 alpha decays make it powerful tool for cancer therapy
- Highest priority isotope in DOE/NSAC isotope review
- Cross sections for production from ^{232}Th are not well known – disagree with calculations
- New measurements of ^{225}Ac production from ^{232}Th have been made at LANSCE/WNR at 800 MeV via spallation, at 200 MeV using stacked foils, and at 100 MeV at the IPF.



The role of grain boundaries in modifying radiation damage evolution in simple metals

X. Bai, MST-8; A. Voter, T-1; R. Hoagland, MST-8; M. Nastasi, MPA-CINT; B. Uberuaga, MST-8

Introduction & Methods

Nuclear energy is the one green energy source that can have immediate impact on climate change. However, the intense irradiation produces significant damage in materials, primarily in the form of interstitials and vacancies, that make harnessing the full potential of nuclear energy challenging. The aggregation of such point defects can lead to swelling (A), embrittlement, amorphization, and hardening of materials, which severely affect the reliability and lifespan of nuclear energy systems.

It has been long realized that grain boundaries (GBs) and interfaces are effective sinks for defects (B). However, how defects interact with GBs at the atomic scale is far from clear.

To investigate the defect-GB interaction mechanisms, this work addresses the following questions:

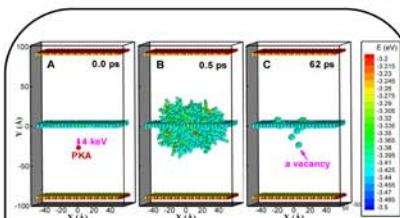
- How do GBs affect defect production.
- Does the specific GB structure make a difference in defect production.
- How do vacancies evolve over long time scales near GBs (aggregation or annihilation).
- Are there any unknown interaction mechanisms between GBs and defects.

Radiation damage is a multi-time scale problem. Three atomistic modeling methods that span different time scales are used in this study:

- Molecular dynamics (MD) is used for investigating defect production at the picosecond (ps) time scale.
- Temperature accelerated dynamics (TAD) is used for studying defect annealing at the microsecond (μ s) time scale.
- Molecular statics is used for calculating the equilibrium thermodynamic properties.

Results & Discussion

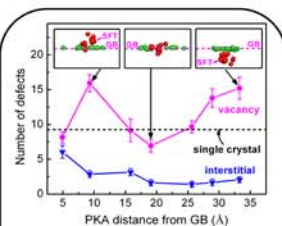
MD Simulations of Collision Cascade Induced Damage Near GBs



MD simulations were performed to investigate how GBs affect the defect production at the ps time scale. Here we show a representative MD simulation of a collision cascade near a $\Sigma 11$ symmetric tilt GB at 300 K. Atoms are colored by their potential energy and only defective (energy > 3.43 eV) and boundary atoms are shown.

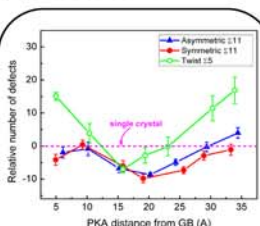
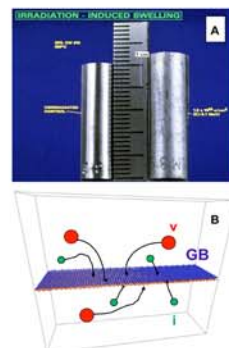
- (A): The initial 4-keV primary knock-on atom (PKA) is 25 Å below the GB.
- (B): The cascade reaches its maximum size.
- (C): The cascade cools down. Some vacancies remaining below and above the GB. Note that in this display scheme, a vacancy is characterized as a 12-atom cluster.

This simulation shows that interstitials are loaded into the GB while vacancies remain in the bulk after a collision cascade occurs.



Defect production is strongly affected by the presence of the $\Sigma 11$ symmetric tilt GB:

- The number of surviving interstitials (average of 15 runs) is much less than in the single crystal.
- The number of residual vacancies is either close to or greater than in the single crystal.
- The optimal distance is 20 Å.
- As the insets show, most interstitials (green) are loaded to the GB; vacancies (red) may preferentially reside above, within, or below the GB depending on the initial PKA distance.
- Stacking fault tetrahedra (SFT) are often observed when the PKA is not at the optimal distance.



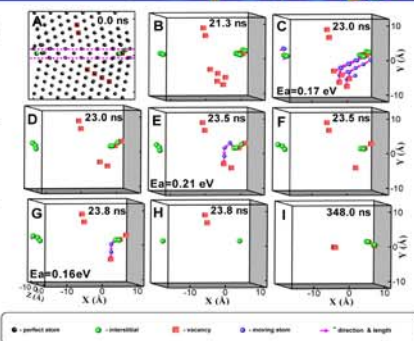
Comparison of the total number of defects (v+i) produced near a $\Sigma 11$ symmetric tilt GB, a $\Sigma 11$ asymmetric tilt GB, and a $\Sigma 5$ twist GB:

- The optimum PKA distance for each GB is around 20 Å.
- In general, the number of surviving defects follows a "U" shape.
- Both $\Sigma 11$ symmetric and asymmetric tilt GBs reduce defect production more than the $\Sigma 5$ twist GB.
- The specific GB structure affects defect production, but the overall trend is similar.

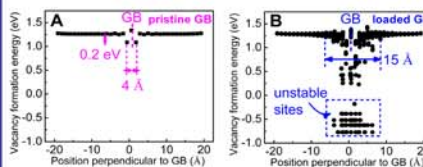
TAD Simulations of Defect Annealing Near GBs Over Long Time Scale

After the defect production stage, interstitials are loaded into the GB while vacancies remain in the bulk region. The key question is how these defects evolve over long time scales. Here we show damage annealing processes near a $\Sigma 11$ symmetric tilt GB as simulated with TAD:

- A: Initial cascade-induced damage structure from MD.
- B: The five vacancies below the GB form a cluster at 21.3 ns.
- C & D: Surprisingly, at 23 ns, three interstitials emit from the GB to annihilate three vacancies with a barrier of 0.17 eV, much smaller than the vacancy diffusion barrier in bulk, 0.69 eV.
- E & F: Another interstitial emission event at 23.5 ns with a barrier of 0.21 eV.
- G & H: The last interstitial emission event at 23.8 ns with a barrier of 0.16 eV.
- I: The remaining two vacancies diffuse to the GB via the slower hopping mechanism. At 348.0 ns, all defects are annihilated or absorbed by the GB.



Molecular Statics Calculations of Defect Thermodynamics Near GBs



The thermodynamics of defects near GBs change significantly when the GBs are loaded with interstitials, the typical damage structure after a cascade:

• (A): At the pristine $\Sigma 11$ symmetric tilt GB, the vacancy formation energy decreases only slightly – 0.2 eV – from the bulk value.

• (B): At the GB loaded with 10 interstitials, the vacancy energy profile changes significantly: unstable vacancy sites appear, corresponding to barrier-free interstitial emission. Low-barrier interstitial emissions are also found at the 1st and 2nd nearest neighbors of unstable sites.

Similar results are observed for a $\Sigma 11$ asymmetric GB, $\Sigma 5$ twist GB, and a combined asymmetric tilt+twist GB.

Comparison with Experiment

Chimi et al (JNM 297, 355 (2001)) irradiated large vs small (~20 nm) grained Au. Their observations correlate well with our simulation results.

- At low T, nano-Au accumulated damage faster than poly-Au. Our MD simulations show the boundaries trap interstitials, inhibiting recombination if no thermal annealing can occur.
- At high T, nano-Au behaves better than poly-Au. At this temperature, vacancies can directly diffuse to the boundary, recombining with the trapped interstitials. There are more sinks for both types of defects and recombination is enhanced.
- At intermediate T, nano-Au recovers from the damage faster than poly-Au, even at temperatures where vacancy diffusion cannot occur. A small barrier process, such as interstitial emission, must be active to explain that enhanced recovery.

Conclusions

Using three multi-time scale modeling methods, we have examined defect production and annealing near GBs. We find:

- During defect production, GBs preferentially absorb interstitials over vacancies. An optimal PKA distance from the GB exists.
- The two $\Sigma 11$ tilt GBs produce less defects than the $\Sigma 5$ twist GB. Thus, the specific GB structure affects defect production. However, the overall trend of GB effects in the defect production is similar.
- A new and counterintuitive defect recombination mechanism, interstitial emission from damaged GBs, is found. It typically has a much lower barrier than vacancy diffusion. This mechanism helps explain why nanocrystalline materials [1] have better or worse radiation tolerance than their polycrystalline counterpart at different temperatures.
- Work underway in EFRC/CMIME to understand role of boundaries in Cu on shock response.

Acknowledgements:





Atomistic modeling and experimental studies of the shock response of Cu/Nb nanolayered composites

T.C. Germann, T-1; R.F. Zhang, T-3; J. Wang, X.-Y. Liu, MST-8; S.N. Luo, P-25; W.Z. Han, P-24; I.J. Beyerlein, T-3; A. Misra, MPA-CINT

Abstract

Classical molecular dynamics (MD) simulations and laser and gas gun experiments are used to study the shock response of Cu-Nb nanolayered composites. Previous work has demonstrated the unusual radiation tolerance and mechanical strength of such materials due to the ability of Cu/Nb heterointerfaces to absorb both *point defects* (thus catalyzing Frenkel pair recombination) and *line defects* (by delocalizing them at the easily sheared interfaces), respectively. Initial laser experiments and MD simulations indicate that shock-induced defects in Cu/Nb nanolaminates are largely recovered upon unloading due to the confinement of plasticity (slip or twinning) within the layers, and the ability of interfaces to absorb dislocations. Here we describe the development of an embedded atom method (EAM) interatomic potential which provides an accurate description of deformation twinning in bcc Nb under compression, slip in fcc Cu, and the interface structure of Cu-Nb interfaces with the Kurdjumov-Sachs (KS) orientation relationship. Using this potential, MD simulations provide insight into the role of atomic Cu-Nb interface structures on the nucleation, transmission, absorption, and storage of dislocations during shock loading. The key role which interface structure plays is demonstrated by post-mortem transmission electron microscopy (TEM) of shock-recovered samples, which indicate that deformation twinning in Cu is preferentially nucleated from Cu(112)/Nb(112) interface habit planes; corresponding MD simulations are underway.

Motivation

Previous work at LANL has demonstrated that nanoscale metallic multilayers synthesized via physical vapor deposition exhibit remarkable properties:

- Radiation tolerance due to ability of interfaces to absorb point defects and catalyze Frenkel pair recombination [1]
- Ultrahigh strength under quasistatic mechanical loading, e.g. nanopillar compression

These properties may lead to unique behavior under dynamic loading, if interfaces can absorb line defects (dislocations) produced by shocks.

Experimental Methods

Shock experiments with both laser and gas gun drivers are being used:

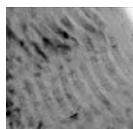
- Laser experiments allow thin (10-100 μm) samples, 10^7 - $10^9/\text{s}$ strain rates
- Gas gun experiments (10^7 - $10^9/\text{s}$) can utilize either sandwiched foils or bulk nanolayer samples synthesized by other techniques

Post mortem analysis of shock-recovered samples via high resolution transmission electron microscopy provides detailed information on the final deformation structures (e.g. slip, twinning, phase transformations), but no information on *when* deformation took place (e.g. during shock compression or unloading), nor on any transient intermediate states.

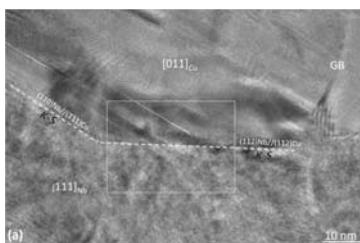
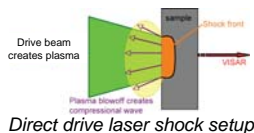
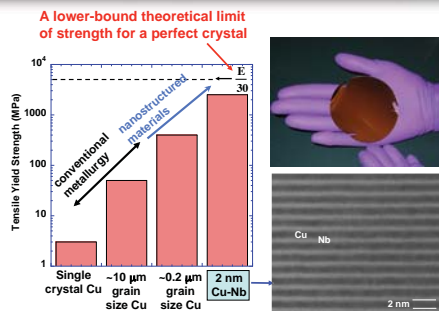
Experimental Results

In contrast to the abundant dislocation activity seen in pure Cu or Nb single crystals at identical conditions, Cu/Nb nanolaminates respond differently:

- Little if any damage seen in very thin layers (e.g. 5nm)
- Deformation twinning in Cu layers of thicker samples (e.g. 30 nm), with preferential nucleation from Cu(112)/Nb(112) interface habit planes



No damage evident in 5 nm Cu / 5 nm Nb nanolaminate after ~6 GPa laser shock



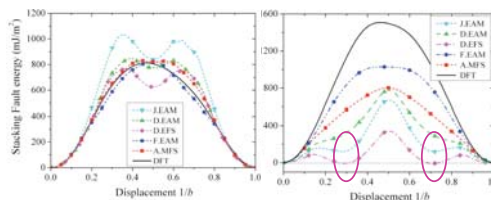
High-resolution TEM showing deformation twins near a shocked interface in a 30 nm Cu / 30 nm Nb nanolaminate.

Cu/Nb Interatomic Potential Development

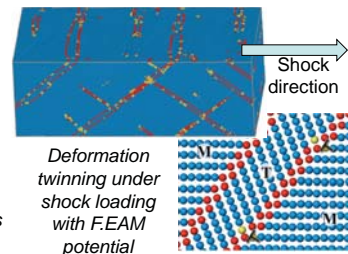
Many existing potentials for bcc metals such as Nb exhibit artificial structural phase transformations under high pressure, and are thus unsuitable for shock compression studies [3].

We have shown that the origin can be traced to artificial minima in the high-pressure γ -surfaces [4].

A new Cu/Nb interatomic potential has been constructed that accurately describes both Cu/Nb interface structure and the high-pressure response of the Cu and Nb constituents [5].

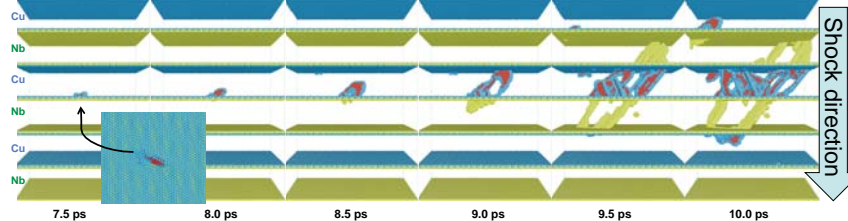


{112}<111> γ -surfaces for several Nb interatomic potentials and from density functional theory (DFT) at zero pressure (left) and 50 GPa hydrostatic pressure (right).



Dislocation Emission, Transmission, and Absorption by Interfaces

Molecular dynamics simulations of shocked Cu/Nb nanolayers with Cu(111)/Nb(110) KS interface structure reveal details of the (slip and twinning) dislocation emission, transmission, and absorption at interfaces. As seen below, the interface pattern controls the dislocation emission, and preferred slip system evolve along directions with high linear density of misfit dislocation intersections. Dislocations transmit first from a Cu {111} slip plane onto a Nb {110} plane, and subsequently into the neighboring Cu {111} plane. Crystal orientation is the key factor to control the dislocation transmission, transmission process try to locate at the neighbor slip planes with the smallest angle.



Dislocation nucleation and transmission at Cu/Nb interfaces in a shocked Cu/Nb nanolaminate (Cu 5nm / Nb 5nm, Kurdjumov-Sachs interface structure, $u_p = 650\text{m/s}$, $T_0 = 300\text{K}$, SPaSM code)

Ongoing and Future Work

We are examining the effect of interface structure using both simulation and experiment, focusing on other interface structures such as Cu(112)/Nb(112) that are produced by severe plastic deformation techniques such as accumulative roll bonding (ARB).

- [1] X. Zhang, E. G. Fu, A. Misra, and M. J. Demkowicz, "Interface-enabled Defect Reduction in He Ion Irradiated Metallic Multilayers," *JOM* **62**, 75 (2010).
- [2] W. Z. Han, A. Misra, N. A. Mara, T. C. Germann, J. K. Baldwin and S. N. Luo, "Role of interfaces in shock-induced plasticity in Cu/Nb nanolaminates," submitted to *Phil. Mag.*
- [3] T. C. Germann, "Large-scale classical molecular dynamics simulations of shock-induced plasticity in BCC niobium," in *Shock Compression of Condensed Matter - 2009*, M. L. Elert, W. T. Buttler, M. D. Furnish, W. W. Anderson, and W. G. Froude, eds. (AIP Conference Proceedings Vol. 1195, Melville, NY), pp. 761-764.
- [4] R. F. Zhang, J. Wang, I. J. Beyerlein, and T. C. Germann, "Twinning in BCC metals under shock loading: a challenge to empirical potentials," submitted to *Phys. Rev. Lett.*
- [5] X.-Y. Liu *et al.*, to be published.





Irradiation damage effects in ceramic oxides induced by high temperature and high fluence ion beam irradiation

I. Usov, D. Devlin, MST-7; J. Won, M. Hawley, MST-8; A. Suvorova, Univ. of Western Australia; Y. Wang, K. Sickafus, MST-8

Introduction

Radiation tolerant ceramic oxides are considered to be attractive for various nuclear energy applications (for both fission and fusion type reactors). An important criterion for selection of suitable materials is their tolerance to a combination of irradiation-induced damage and elevated temperature. A major cause of radiation damage in nuclear reactor components is the stopping of fast neutrons, fission fragments, high-energy alpha particles and recoil nuclei formed following alpha decay. To simulate a nuclear reactor radiation environment, we have employed ion beam irradiation. A common feature of the ion irradiation is that ions can penetrate only to a particular depth; therefore, the nature of ion irradiation-induced defects substantially depends on the surface proximity. In this poster, we present an experimental study of ion irradiation-induced damage effects in various ceramic oxides. Particular attention is given to the high dose and high temperature effects on modification of both near surface and bulk properties.

This work is motivated by our goal to understand the mechanisms responsible for irradiation-induced defects, including nucleation, growth and recovery. Our ultimate objective is to discover ceramic oxides resistant to irradiation.

This work is supported by (i) the US Department of Energy (DOE), Office of Basic Energy Sciences (OBES), Division of Materials Sciences; (ii) a Laboratory Directed Research and Development (LDRD DR) grant and (iii) a US DOE Advanced Fuel Cycle Campaign and Fuel Cycle R&D Program. Ion irradiation and Rutherford backscattering (RBS) analyses were performed in the Ion Beam Materials Laboratory (IBML) at LANL. Transmission electron microscopy (TEM) was performed in the Electron Microscopy Laboratory (EML) at LANL, as well as the Center for Microscopy Characterization and Microanalysis at the University of Western Australia.

Experimental details: Ion Beam Materials Laboratory (IBML)

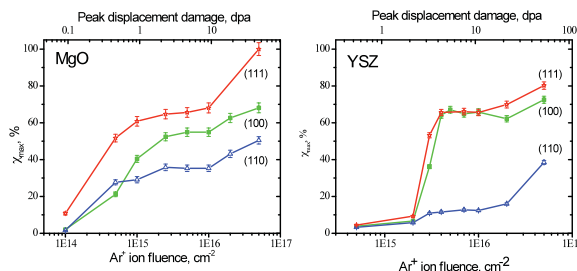


A medium energy ion irradiation setup has been installed on the 15° beam line on the 3.2 MV NEC Tandem accelerator in the IBML. A typical ion beam used for the radiation damage studies is 10 MeV Au³⁺ or 2 MeV Si⁺. The ion irradiation can be performed over a wide temperature range from 90 to 1400 K. The standard irradiation area, which provides enough material for various characterization techniques, is 12 x 12 mm². A low energy ion irradiation was performed by 200 keV Varian ion implanter.

For more details see
I.O. Usov et al. Nucl. Instr. Meth. B 267 (2009) 1918
I.O. Usov et al. Nucl. Instr. Meth. B (2011), in press

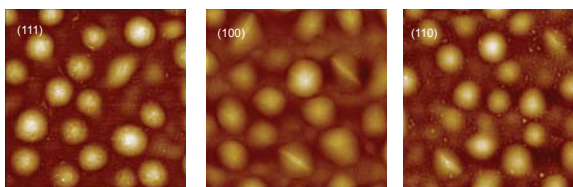
Experimental results

Ion Fluence Effect



Damage accumulation fraction ($\langle A \rangle_{\max}$) versus Ar⁺ ion fluence for magnesium oxide (MgO) and yttria-stabilized zirconia (YSZ) single crystals with surfaces oriented along three major low-index crystallographic directions. Damage evolution with increasing ion fluence proceeded via several characteristic stages and the total damage exhibited a strong dependence on crystallographic orientation.

I.O. Usov et al. Nucl. Instr. Meth. B 268 (2010) 622

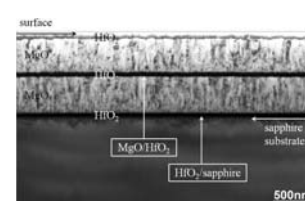


Atomic force microscopy (AFM) micrographs (5 μm x 5 μm field-of-view) images obtained from three low-index YSZ single crystal surfaces irradiated with 150 keV Ar⁺ (1x10¹⁷ cm⁻², equivalent to 100 displacements per atom or dpa). Note aligned cracks in elongated blisters on the (100) and (110) surfaces and peeling of material off the hillocks on the (111) surface.



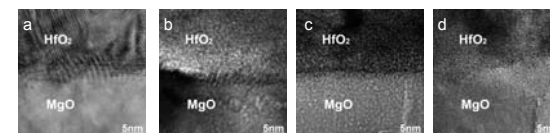
Cross-sectional TEM images obtained from three low-index YSZ single crystals irradiated with 150 keV Ar⁺ (1x10¹⁷ cm⁻², equivalent to 100 dpa). The microstructure in the near surface region consists of flat, Ar-filled cavities. The cavities dimensions depend on the surface orientation and correlate with the fractional damage determined by RBS measurements: larger cavities are observed in (111) YSZ, versus smaller ones in (100) and (110) YSZ.

Irradiation Temperature Effect

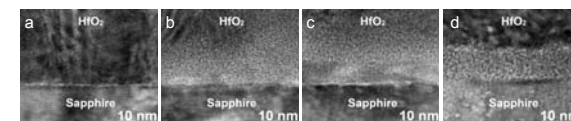


Cross-sectional TEM micrograph obtained from an as-deposited, penta-layer structure, HfO₂/MgO/HfO₂/MgO/HfO₂, on an (0001) sapphire substrate. This multi-layer structure was designed to mimic a CERCER (ceramic-ceramic) composite fuel form. The MgO is intended

to represent a non-fissile component, while the HfO₂ is a surrogate for a fissile phase. The goal of this study was to investigate features of radiation damage evolution in a wide irradiation temperature range, spanning from 90 to 800 K. The location of the MgO/HfO₂ and HfO₂/sapphire interfaces to be discussed further discussed below, are labeled with arrows.



HRTEM images obtained from the MgO/HfO₂ interface region before irradiation (a) and after irradiation with 10 MeV Au ions to a fluence of 5x10¹⁵ Au/cm² (equivalent to 13 dpa in HfO₂ and 7 dpa in MgO) at various temperatures: 90 K (b), 300 K (c) and 800 K (d). The following sequential microstructural changes are observed at the interface: crystalline (as-deposited) → amorphous (90 K) → amorphous and crystalline mixture (300 K) → crystalline (800 K). To our knowledge, bulk MgO and HfO₂ do not amorphize when they are irradiated individually. On the other hand, in a composite structure, amorphization seems to be possible.



HRTEM images obtained from the HfO₂/sapphire substrate interface region before irradiation (a) and after irradiation with 10 MeV Au ions to a fluence of 5x10¹⁵ Au/cm² (equivalent to 18 dpa in HfO₂ and 10 dpa in sapphire) at various temperatures: 90 K (b), 300 K (c) and 800 K (d). Microstructural evolution at the sapphire interface region differs substantially from the irradiation-induced changes observed in the MgO and HfO₂ interfacial regions (shown above). Surprisingly, we find exceptional amorphization resistance at low temperature, then a tendency towards amorphization with increasing temperature: crystalline (as-deposited) → crystalline (90 K) → amorphous and crystalline mixture (300 K) → amorphous (800 K).



Advanced Materials Development and Testing for Fuel Cycle Research & Development Program

O. Anderoglu, MST-8; J. Van den Bosch, SCK-CEN, Belgium; T. Saleh, MST-16; B.H. Sencer, INL; P. Dickerson, R. Dickerson, MST-6; P. Hosemann, UC Berkeley; G.R. Odette, N. Cunningham, Y. Wu, UC Santa Barbara; D. Hoelzer, ORNL; B. Wirth, U of Tennessee; A. Misra, M. Nastasi, MPA-CINT; S. Maloy, SPO-CNP

Abstract

One of the main objectives of the fuel cycle research and development program is to develop core materials that can withstand irradiation damage up to or greater than 400 dpa. This will facilitate high burn up of the fuel ($\geq 40\%$) which in turn reduces the waste while producing zero carbon emission electricity.

The materials under study include nanostructured ferritic alloys (NFA's) (e.g. 14YWT), Fe based model alloys, and ferritic/martensitic (F/M) alloys (e.g. HT-9 and T91). F/M alloys were previously irradiated in the fast flux test facility (FFTF) reactor to doses up to 184 dpa at irradiation temperatures from 380-546 °C. This also includes analysis of a duct made of HT-9 after irradiation to a total dose of 155 dpa at temperatures from 410 to 470 °C with lower dose material covering irradiation temperatures from 370 to 510 °C.

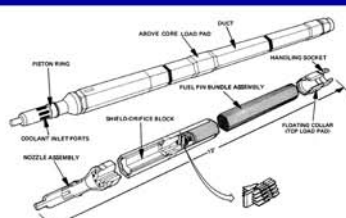
In addition to optimization of the microstructure in large heats, the comprehensive study on NFA's includes initial ion beam irradiations, processing studies to manufacture thin walled tubing for cladding and appropriate welding techniques for joining.

As a complement to engineering studies on NFA's, research is underway on model alloys focusing on the crystal structure at the atomic level and phase and interface stability under irradiation of the oxide-metal interfaces. The studies on the advanced materials utilize advanced characterization techniques including transmission electron microscopy (TEM), atom probe tomography (LEAP), and Small Angle Neutron Scattering (SANS).

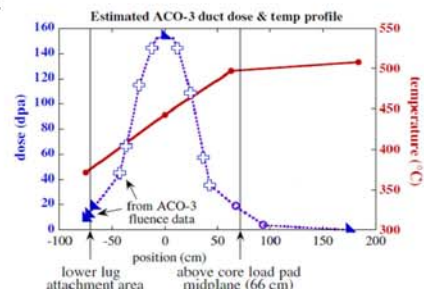
Experimental Details



Fast flux test facility, Hanford site, WA. ACO-3 duct was irradiated in the sodium cooled fast reactor for about 6 years.



Schematic of the ACO-3 duct. Both the duct and the clad are made out of HT-9.



	C	N	Cr	Mo	Mn	Si	Ni	V	Nb	W	Ta
HT-9	0.21	-	11.8	1.03	0.50	0.21	0.51	0.33	-	0.52	-
T-91	0.08	0.054	8.6	0.89	0.37	0.11	0.09	0.21	0.072	-	-
HT-9M	0.15	0.018	10.2	1.27	0.48	0.06	0.44	0.19	-	-	0.17

Results and Discussion

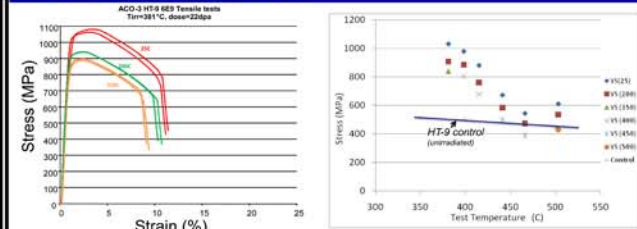


Fig 1. Very little change in yield stress is observed for the samples irradiated at $>443^{\circ}\text{C}$ while a significant increase is observed after irradiation at 381°C .

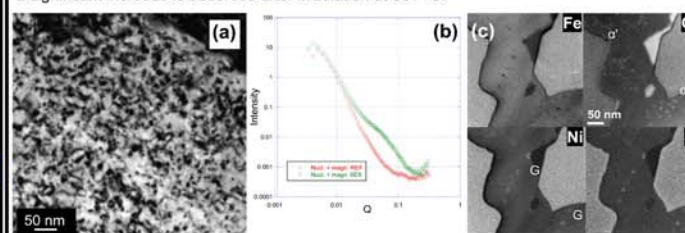


Fig 2. 20 dpa 380°C zone: (a) TEM image $g=(200)$ shows precipitates, loops and dislocations. (b) SANS measurement indicates presence of second phase particles. (c) EFTEM jump ratio images show both Cr rich α' (7.8 nm, 1.8%) and G-phase precipitates (11.3 nm, 0.8%) that are identified to be $\text{Mn}_6\text{Ni}_{16}\text{Si}_7$ using EDX.

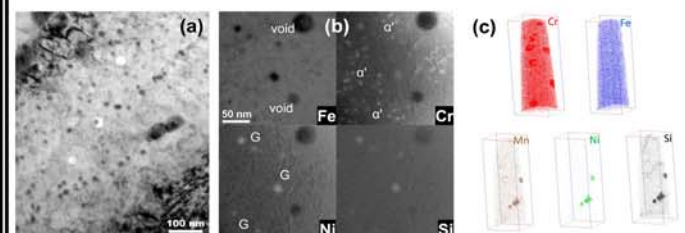


Fig 3. 100 dpa 410°C zone: (a) TEM image shows G-phase precipitates and voids (24 nm). (b) EFTEM jump ratio images show both α' (9 nm, 0.1%) and G phase (16.2 nm, 0.3%). (c) LEAP re-constructions show more details of the shape of α' precipitates.

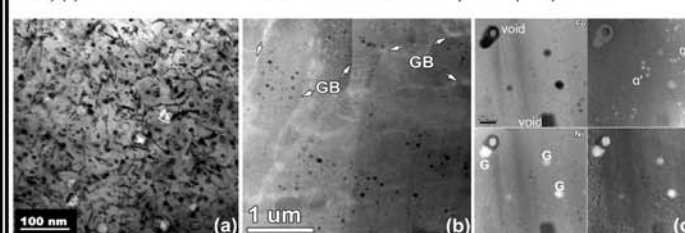


Fig 4. 155 dpa 440°C zone: (a) TEM image shows G-phase precipitates and voids. (b) Average void size ~ 28 nm, volumetric swelling based on observed voids is 0.3%. (c) EFTEM jump ratio images show both α' (9.6nm, 0.44%) and G phase precipitates (26.5nm, 1.1%).

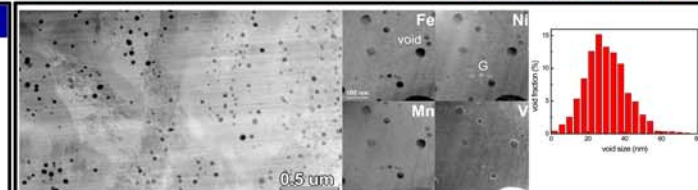
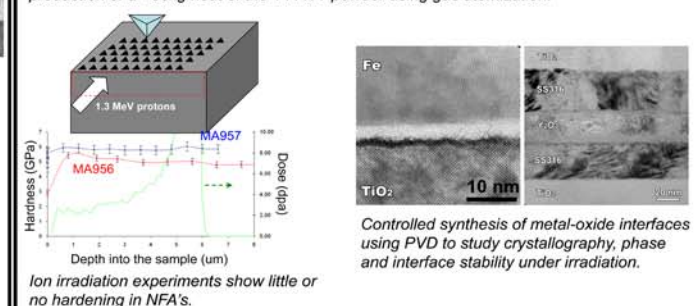
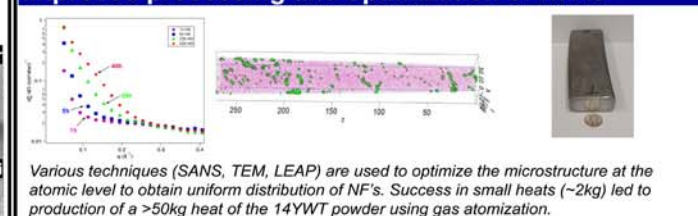


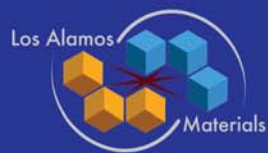
Fig 5. 184 dpa 413°C (T-91): Average void size ~ 29 nm, volumetric swelling based on observed voids is 1.6%. EFTEM jump ratio images show G-phase precipitates.

Improved processing and optimization of NFAs



Summary

- An HT-9 hexagonal duct was examined following about 6-year irradiation campaign of a fuel assembly to a total dose of 155 dpa in the FFTF.
- Yield stress is a strong function of irradiation temperature and very little hardening was observed for irradiation $\geq 430^{\circ}\text{C}$.
- HT-9 retained its swelling resistance reaching $\sim 0.3\%$ at 155 dpa. A high density of uniformly distributed precipitates and point defect clusters at $410^{\circ}\text{C} \leq$ is responsible from significant increase in yield strength.
- The data obtained will help both to develop models that will predict radiation effects in core materials and to produce advanced alloys more resistant to irradiation.
- The optimized processing parameters on the initial batch of NFAs showed significant ion-irradiation resistance. Atomic level characterization of the metal-oxide interface and phase stability studies are in progress.



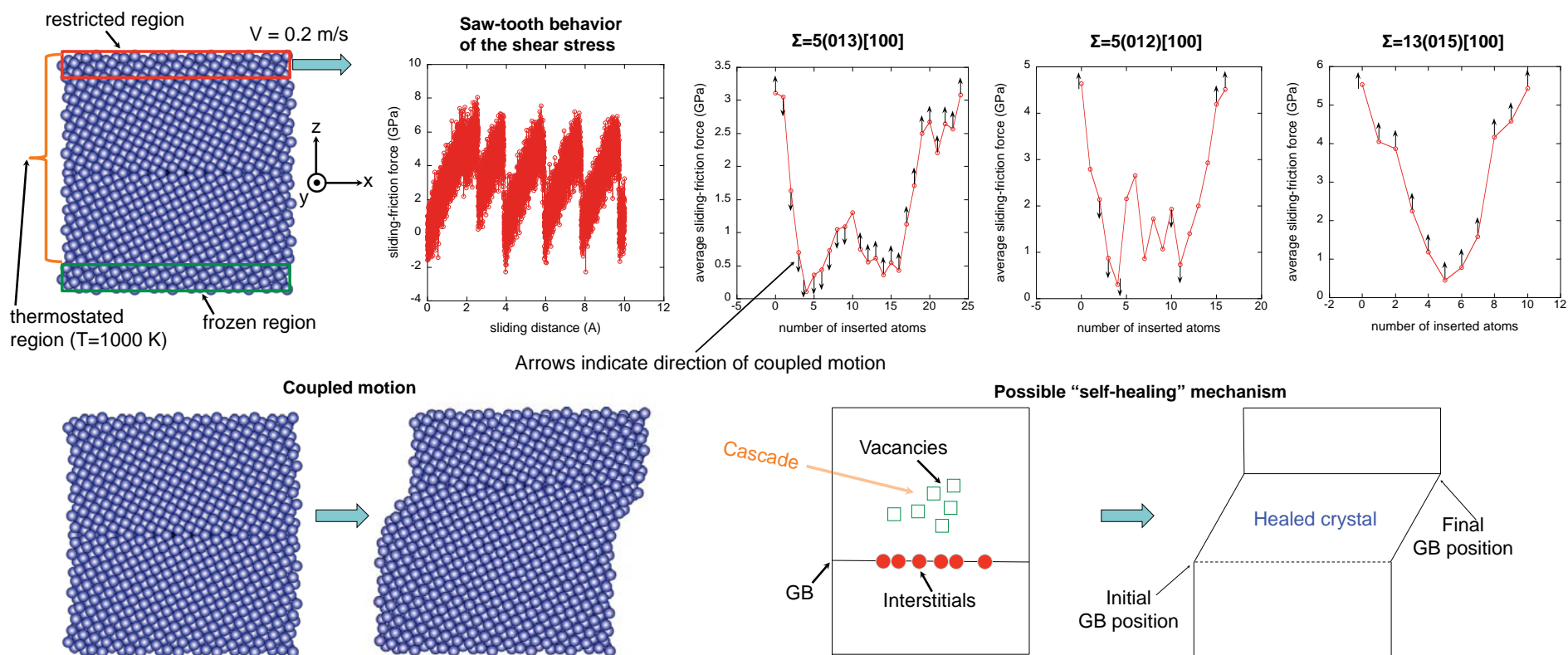
Influence of interstitials or vacancies on grain boundary sliding processes in bcc tungsten

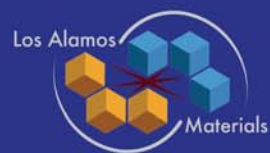
V. Borovikov, D. Perez, X. Tang, T-1; X.-M. Bai, B.P. Uberuaga, MST-8; A.F. Voter, T-1

Abstract

Atomistic computer simulations were performed to study the influence of radiation-induced damage on grain boundary (GB) sliding process in bcc tungsten (W). For a number of GBs, we found the surprising result that introducing interstitials or vacancies into GB can reduce the average sliding-friction force under shear by more than an order of magnitude. Moreover, because these GBs typically shear in a well-known "coupled" way, we speculate that this may provide W with a built-in "self-healing" capability under irradiation conditions, as follows. A collision cascade produces vacancies and highly mobile interstitials; the diffusing interstitials find, and are trapped at, a nearby GB. The interstitial-loaded GB is now so easy to shear that internal stresses in the crystal may start it moving, and the coupled motion causes it to sweep past the cascade center, sweeping up the vacancies as it goes. We have also observed that as the number of interstitials in the GB is varied, the direction of the coupled motion sometimes reverses, causing the GB to sweep in the opposite direction under the same applied shear stress.

Model, Results & Discussion



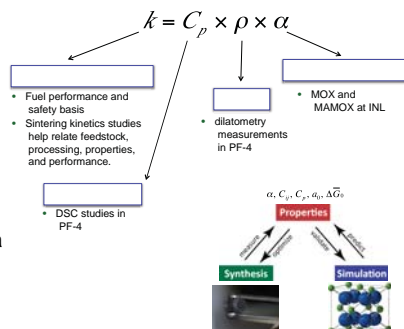


Sintering of mixed-oxide fuel pellets

J. Mitchell, M. Chavez, MST-16; S. Willson, MET-1; K. McClellan, MST-8

Overview

We are measuring the thermophysical properties of mixed-oxide (MOX) and minor actinide-bearing MOX (MAMOX) fuel pellets in support of the Fuel Cycle Research & Development Program (FCR&D). To better understand these properties and how they are impacted by processing, we have been studying the sintering behavior of pellets as a function of temperature and atmosphere. We show here results for in situ sintering in a dilatometer and dimensional changes measured following interrupted sintering.



Pellet Fabrication

	starting weights (g)				oxide fractions			
	PuO ₂	dUO ₂	AmO ₂	NpO ₂	PuO ₂	dUO ₂	AmO ₂	NpO ₂
FY10802011	5	20	0	0	20	80	0	0
FY10703011	7.5	17.5	0	0	30	70	0	0
FY10MA802011	5	18.8	0.75	0.5	20	75	3	2
FY10MA703011	7.5	16.3	0.75	0.5	30	65	3	2

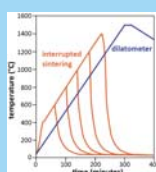


dilatometer samples

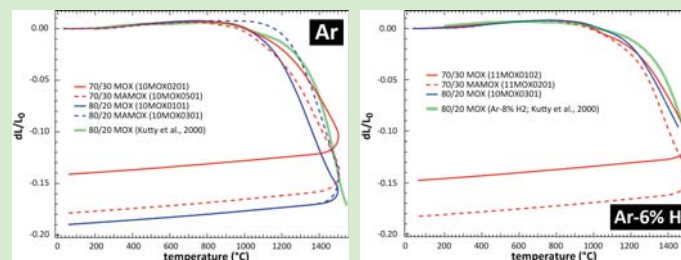
- powders SPEX milled for 15 minutes
- milled powders pressed into 1.3 g pellets in 0.235" die @ 120 MPa for 10 seconds
- polyethylene glycol binder burned out at 450 °C for 4 hours (Ar atmosphere)

interrupted sintering also includes

- measure pellet dimensions
- heat at 20 °C/min to 400 °C
- heat at 5 °C/min to temperature of interest (600, 800, 1200, 1400 °C)
- remove and measure pellet dimensions



Dilatometry Results



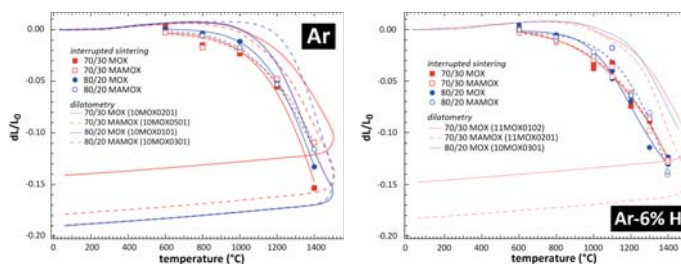
Sintering in Ar slightly increases kinetics.

Sintering curves similar to results of Kutty et al. (2000)

Theoretical densities start at ~45% and finish at ~80%.

High number of furnace failures make systematic comparison difficult.

Interrupted Sintering



Interrupted sintering measurements suggest onset at earlier temperature than dilatometry.

Differences in additional ramp rate to 400 °C may be cause of comparatively early sintering onset.

Dilatometry

Ar glovebox (~0.5 % O₂) in TA-55, PF-4

- frequent unexpected SiC furnace element failures (3 in 18 months)
- two thermocouple failures
- manufacturer redesigned Rh furnace for future high-temperature work

furnace environment

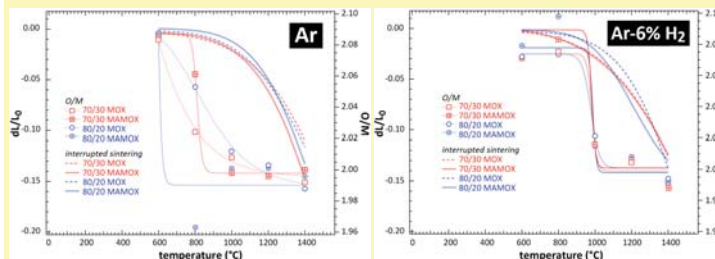
- evacuate with house vacuum (7x10⁻² mbar) and backfill with UHP Ar three times
- dynamic atmosphere with 30 ml/min UHP Ar (~5 ppm O₂) or Ar-6% H₂

temperature profile

- heat: 30 °C to 1500 °C, 5 °C/min
- isothermal: 5 min
- cool: 2 °C/min to 30 °C



O/M Changes During Sintering



Pellets start off hyperstoichiometric and finish at or slightly hypostoichiometric.

Sintering in Ar results in more rapid O/M



Plutonium Science and Research Strategy: Use of Special Isotopes – ^{242}Pu

D. L. Clark, Institutes Office; E. D. Bauer, MPA-CMMS; D. S. Peterson, MST-7

Abstract

Under the NNSA Complex Transformation, Los Alamos National Laboratory was named a consolidated Center of Excellence for plutonium research, development, and manufacturing activities. In response, the Laboratory has developed an institutional plutonium science strategy that defines research needs and opportunities that share a common underpinning of Los Alamos missions in nuclear deterrence, global threat reduction, and energy security. One of our 14 objectives is to establish a small-scale plutonium research and development effort using plutonium-242 and other scarce and unique materials and isotopes.

Background

Having a sixteen times lower specific activity than Pu-239, meaningful quantities of Pu-242 metal, alloys and compounds can be used in radiological facilities that function under lower security and lower hazard levels than Category I, II, or III facilities.

Radioactive Decay Properties of Selected Plutonium Isotopes

Mass number	Half-life (yr)	Specific Activity (Ci/g)	Decay Mode	Radiation Energy (MeV)		
				α	β	γ
238	87.7	17	α	5.8	0.011	0.0018
239	24,110	0.063	α	5.1	0.0067	
240	6,561	0.23	α	5.2	0.011	0.0017
241	14.35	100	β		0.0052	
242	375,000	0.0040	α	4.9	0.0087	0.0014
244	80,800,000	0.000,018	α	4.6	0.0071	0.0012

Approach

By focusing on unique, low-specific activity isotopes like Pu-242 the whole nature of Pu research can be dramatically improved, with reduced costs and the possibility of not having the specimens change during measurements. It provides the opportunity to engage academic collaborators and make better use of national user facilities for Pu research. It will mandate the ability to recover materials in a cost effective way. Success will demand a coordinated, integrated effort between the chemistry, physics, and materials science communities. New approaches (low-loss technologies) need to be developed and demonstrated to successfully recover and recycle these rare isotopes.

Status

- Laboratory-wide inventory has been evaluated
- ~ 100 g of high isotopic purity material (99.9%) has been identified and obtained for use
- Space in radiological facilities has been identified (TA-35, Bldg 455)
- Glove-box system has been acquired
- Potential sponsors have been identified
- New LDRD efforts have been initiated
- Chemical recovery procedures have been identified
- Workshop on alternate metal preparation methodologies is in planning stages



Glovebox line acquired for Pu-242 effort

Low-loss Technologies

1 Electrochemical formation of Amalgams

- Pu(III) in 1M acetate buffer solution (pH 3.5–4.5) at 100mA/cm² current density at a Hg cathode at 10–15 °C.
- Hg removal by Ar stream at 600 °C leaves PuHg_n (1 ≤ n ≤ 4); residual Hg removal with vacuum melting at 1100 °C.
- 10 g ingots of alpha Pu-238 produced in Russia



Aqueous electrochemical cell showing Pu(III) formation at Cathode

B. Cunningham, *J Inorg Nucl Chem Lett*, **1967**, 3, 373, 445

F. David, *Rev. de Chim. Mineral.*, **1970**, 78, 1

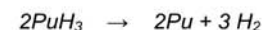
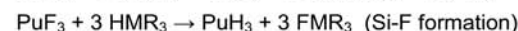
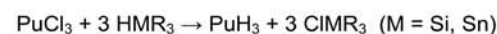
V. Penetrakhin, *Radioanal. Nucl Chem.*, **1990**, 143, 415

V. Penetrakhin, *Proc Int Conf GLOBAL-1995*, (2) Versailles, France, 1716–1724

2 Electroplating from solution

- DMSO demonstrated, ionic liquids under investigation via LDRD project – a variation on current use of electrorefining in molten salts

3 Metathesis Formation of Pu Hydrides



*D.A. Korzekwa, MST-6; J.W. Gibbs, Northwestern U.; D.R. Korzekwa, F.J. Freibert, MST-16;
Telluride Project Team, ASC*

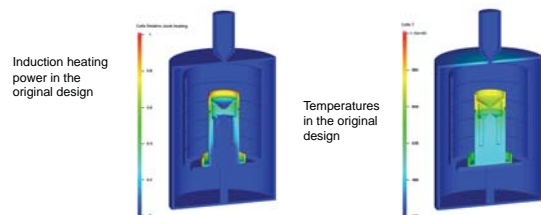
The Truchas code is being developed at LANL to provide a simulation capability for material processing operations such as casting. Truchas development has been funded by the Advanced Simulation and Computing (ASC) program and a variety of nuclear weapons and nuclear energy programs. The features in Truchas are generally tailored for vacuum induction casting of reactive metals such as uranium and plutonium. Primary features include:

- Ability to run large scale 3D simulations on parallel platforms.
- Fluid flow with free surface flow (finite volume)
- Heat transfer with phase change (mimetic finite element formulation)
- Species diffusion (mimetic finite element formulation)
- Small strain solid mechanics (finite volume finite element method)
- Induction heating (Electromagnetic jule heat)
- Radiative heat transfer with view factors (view factors calculated using the Sandia NL code Chaparral)
- Scalable parallel implementation (MPI)
- Written primarily in Fortran 90 (some C, python) for Linux or other unix-like platforms

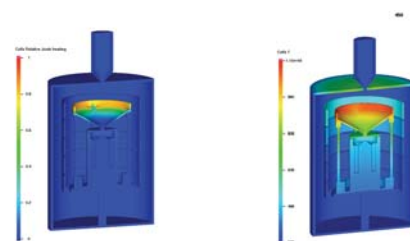
The objective is to produce high quality unalloyed alpha plutonium in sizes that will allow the fabrication of bulk mechanical test specimens. This is a very challenging task because of the very large density changes that accompany the allotropic phase changes in Pu. The primary issue is the 9% volume change that occurs at $\sim 120^{\circ}\text{C}$ during the $\beta \rightarrow \alpha$ transition.

- The large volume changes tend to produce cracks or porosity in the casting
- Numerical simulations with Truchas were used to develop a mold preheating schedule and optimum molten metal temperature
- The strategy was to solidify and cool quickly to the β phase and then cool slowly through the $\beta \rightarrow \alpha$ transition while keeping the transformation front relatively narrow.

Simulation of the induction heating of an initial design based on previous rod molds did not allow the funnel temperature to be hot enough without heating the mold to a much higher temperature than desired.



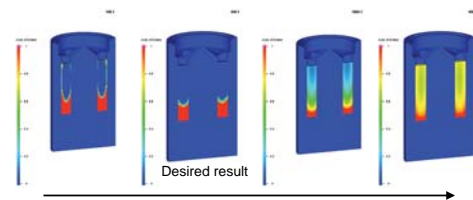
A new design concentrates the induction power in the funnel and separates the funnel from the mold. Simulation of this design showed that the funnel could be kept hot and the mold temperature could be varied by a two step heating cycle.



Induction power and temperatures for the new design

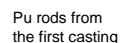
Simulations indicated that it was best to run the induction coil with a relatively small current (250A) until the mold was near the desired temperature then increasing the current to 1000A to rapidly heat the funnel.

Solidification and phase transformation of the Pu was modeled assuming different mold temperatures to find conditions for directional solidification and a narrow solidification front.



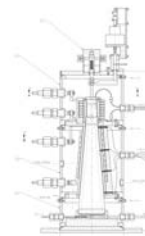
Increasing mold temperature, increasing solidification front width, increasing solidification time

The material produced by this process has fewer defects and a density closer to that expected for pure alpha Pu than other recent attempts.. The predicted thermal histories of the mold match experimental measurements, and work to improve this process is in progress.



Truchas is also being used to simulate a casting process being developed at Idaho National Laboratory for fabrication of metallic nuclear fuels rods. A small bench scale caster (BSC) is being used to evaluate design concepts for casting a uranium-plutonium-zirconium alloy that is a candidate for an advanced metal fuel.

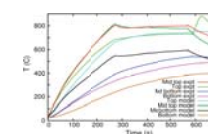
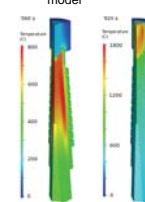
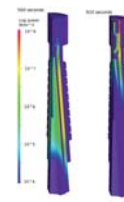
- Three rods 250 mm long by 4.3 mm in diameter
- Induction heated graphite mold and crucible
- Argon atmosphere with optional evacuation of the mold



segment in the
model



Photo courtesy of Randall Fielding, INL



Comparison of model with experimental temperatures

[illegible]

Statistics is independent from the baseline circulation at 570 mm.

Induction heating of the mold and crucible is modeled including radiative heat transfer and conduction. The details of the furnace and mold geometry are captured using a view factor radiation capability. A sensitivity study was conducted to help identify the boundary conditions and material properties that have the largest effect on the temperature field.

Fluid flow, heat transfer and phase change simulations provide insight into aspects of the casting process that cannot easily be observed. Several types of casting defects can be predicted by modeling the solidification behavior.



Snapshot of half symmetry
flow simulation



LEU U-10Mo research reactor fuel development and scale up

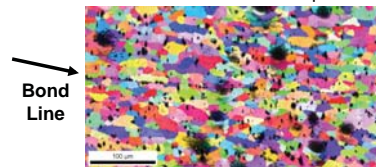
D. Dombrowski, R. Aikin, D. Alexander, A. Clarke, K. Clarke, MST-6; T. Claytor, AET-6; J. Crapps, A. Duffield, P. Dunn, R. Edwards, R. Forsyth, D. Hammon, J. Katz, P. Kennedy, D. Korzekwa, MST-6; N. Mara, MPA-CINT; B. Mihaila, C. Necker, P. Papin, M. Pena, K. Rau, R. Schulze, V. Vargas, R. Weinberg, MST-6

Mission Statement: DOE NA-21 executes a global mission to convert HEU reactors to LEU fuel to reduce the worldwide inventory of weapons usable materials. The NA-21 CONVERT program is developing the supply of special high-density LEU U-10Mo fuel to support these research reactor conversions. This high visibility, schedule driven project will convert U.S. High Performance Research Reactors (NBSR, MTR, ATR, MURR, HFIR) to LEU fuel; NRC reactors to be done by 2015. This project is a collaboration which includes LANL, INL, PNNL, ANL and Y-12.

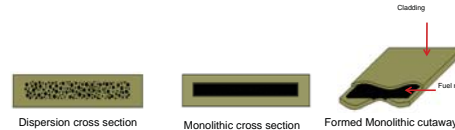
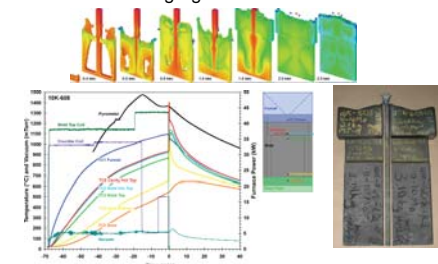
- LANL will perform integrated process scale up, develop alternative process steps and perform advanced characterization, esp. bond strength

Highlights LANL science is contributing to over 14 process step in the baseline process, but here are some contributions with particularly notable impact.

Image Analysis shows fuel miniplates do not have grain growth across Al/Al bond line. New QC method needed for commercial fuel production.



Modeling U-10Mo casting in a book mold to minimize Mo segregation



Goal Replace current dispersion fuel (HEU Oxide or HEU Aluminide with Monolithic U-10Mo Fuel

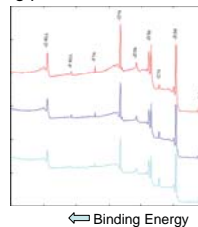
- Up to 8.5 g U-Total/cm³ for LEU dispersion fuel
 - Approximately 1.7 g U-235/cm³
- Up to 16 g U-Total/cm³ in LEU monolithic fuel
 - Approximately 3 g U-235/cm³

Surface Composition How clean is clean? XPS TOA shows effect of different cleaning processes on Zr foil

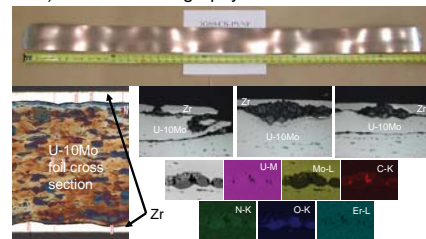
- Relative intensity (compared to Zr peaks) of C increases with decreasing takeoff-angle (TOA) relative to surface plane, indicating presence of top hydrocarbon overlayer.

90° TOA
45° TOA
15° TOA

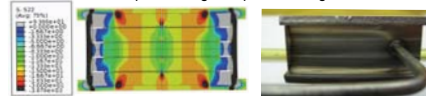
- Note also that F peak intensity decreases with decreasing TOA, indicating that F is associated with the Zr oxide - likely from HF in LANL cleaning process.



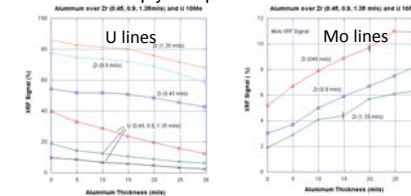
Processing Co-roll and Cold Roll LEU U-10Mo with 800 ppm C content and inclusion stringers. One complete fuel foil obtained per casting coupon - best in program. 3% variation in thickness (U-235 conc) based on radiography



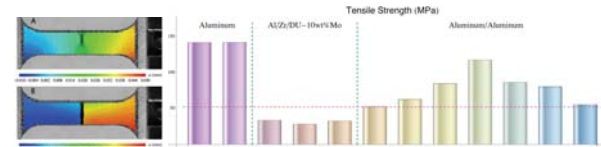
Modeling FEM Modeling of normal stresses and Von Mises stresses in program standard HIP can. Next Step: Modeling of Improved Designs



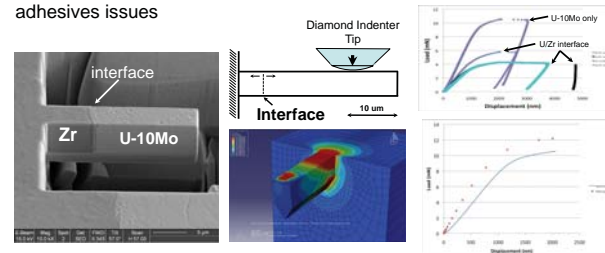
In-Situ Minimum Cladding Thickness Measurements by handheld XRF and UT. This innovation helps achieve MinClad requirements. For Al clad thickness greater than 0.030 in. use portable UT meters, but for clad thinner than 0.030 in. simply use portable XRF meter



Macroscopic Bond Strength Measurements show Al/Al bond strength variation in current HIP can design

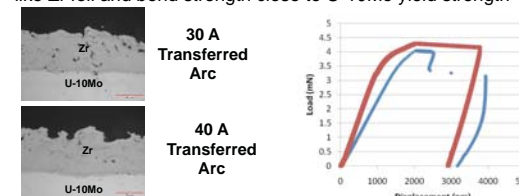


Nanomechanical Bond Strength Measurements performed directly on foils and plates without process variations or adhesives issues



Zr Plasma Spraying as alternate process to co-rolling

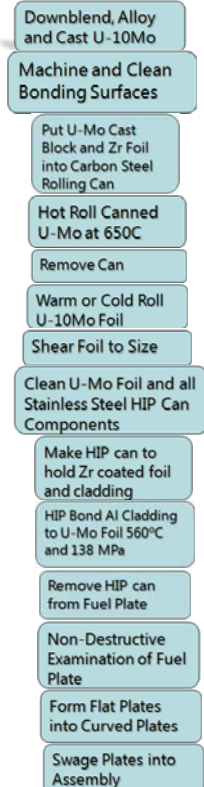
Low Pressure Plasma Spraying of Zr onto U-10Mo shows properties like Zr foil and bond strength close to U-10Mo yield strength



Baseline Process

- Down Blend HEU to LEU by melting and add Mo. Cast.
- Make Zr coated LEU U-10Mo foil (fuel meat) by co-rolling.
 - 0.007 to 0.030 in. thick,
 - 22 - 48 in. long
 - 0.001 in. thick Zr diffusion barrier
- Make fuel plate by diffusion bonding foil using Hot Isostatic Pressing (HIP).
- Form plate to required curvature with soft tooling.

The LANL Sigma Complex is the only US government or industrial site that has all the expertise and existing equipment to make this monolithic LEU U-10Mo fuel plate at pilot scale.

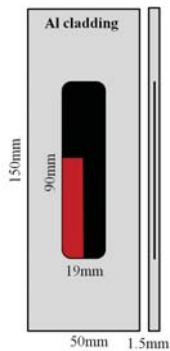




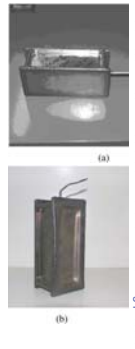
Residual stresses in aluminum-clad uranium-10wt%molybdenum fuel plates

D. Brown, L. Balogh MST-8; B. Clausen LANSCE-LC; M. Okuniewski, INL

Residual Stress in Mini Monolithic U10Mo Fuel Plates

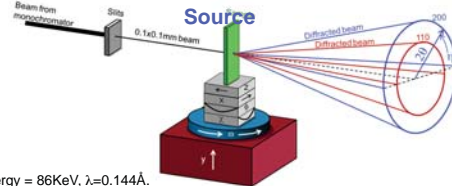


- Funded by the Reduced Enrichment for Research and Test Reactors (RERTR) program.
- Replace HEU with LEU in research reactors.
- Uranium 10wt% molybdenum foil clad with aluminum.
- Residual stresses can cause distortions during processing and use.
- 1.5 mm total
- 0.25mm thick U10Mo foil
- Foil was rolled, annealed, then HIP bonded
- CTE U10Mo $\sim 10 \times 10^{-6}/^{\circ}\text{C}$
- CTE Al $\sim 22 \times 10^{-6}/^{\circ}\text{C}$
 - Expect U10Mo to be in compression
- Diffraction residual stress measurements at the Advanced Photon Source.

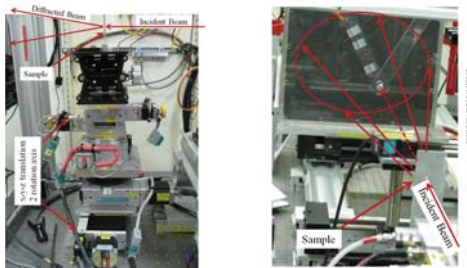


A stainless HIP can - (a) before and (b) after HIP bonding process.

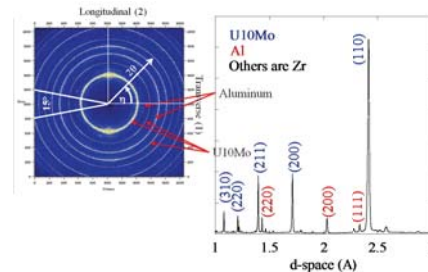
Residual Stress Measurements on 1-ID at Advanced Photon



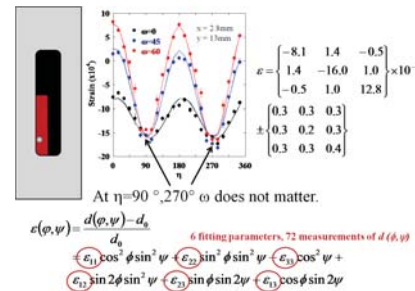
- X-ray energy = 86KeV, $\lambda = 0.144\text{\AA}$.
- Beam cross section : 0.1mm x 0.1 mm
- Collection time at each point 0.7-1.5sec. 4 sec to save data and move sample.
- Ceria standard used for detector calibration
- Measurements at $\omega=0^{\circ}$ (beam normal to sample), 45° , and 60° .



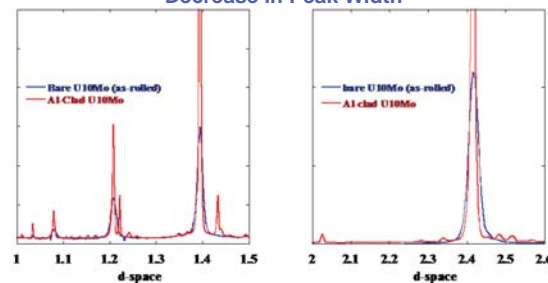
2-D Detector Aids Measurement of Strain Tensor



- Aluminum rings are "spotty" due to larger grains
- Note texture in U10Mo, the (110) is strong along the original rolling direction.
- Rings are "caked" into 24 1-d diffraction patterns.
- $\sim 500,000$ total diffraction patterns.

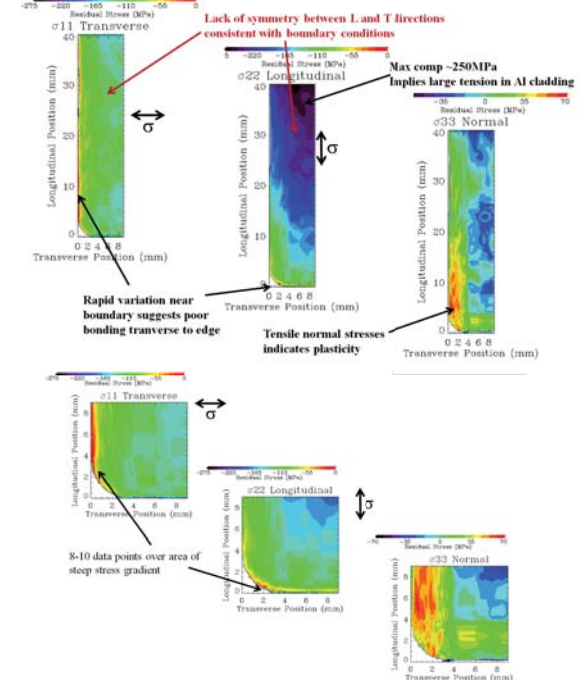


Annealing of U10Mo Foil During Bonding Evident in Decrease in Peak Width



- Narrowing of peak during HIP'ing tells us the microstructure has annealed.
- Bare U10Mo foil $\rho = 60 \times 10^{14}/\text{mm}^2$
- Al-Clad U10Mo $\rho = 6 \times 10^{14}/\text{mm}^2$

Residual Stress Tensor Mapped Over 1/4 of Foil



Summary

- High energy x-rays can be used to characterize microstructure of bulk samples, even with high Z.
 - Demonstrated residual stress, dislocation density, and texture measurements in Al-clad Uranium 10wt% Molybdenum fuel plates.
- ~ 250 MPa compressive residual stress in U10Mo foil.
 - Suggests a yield level tensile stress in Aluminum cladding.
 - Possible sample will distort during subsequent processing steps.
- Tensile residual stress in normal direction indicates plastic deformation (probably in Aluminum) during cooling.
- Rapid approach of transverse components to zero at edges suggests foil is not bonded on lateral edges.
- Asymmetry of stress field (longitudinal vs. transverse directions) is consistent with constraints during HIP'ing.
- Dislocation density of $60 \times 10^{14}/\text{mm}^2$ in as-rolled foil. Reduce by 10x during HIP'ing.
- This data should be used to validate finite element analysis of HIP process.



Chemical segregation of U-10Mo fuel foils during simulated bonding cycles using neutron diffraction

S. Vogel, LANSCE-LC; D. Brown, MST-8; M. Okuniewski, Idaho National Laboratory

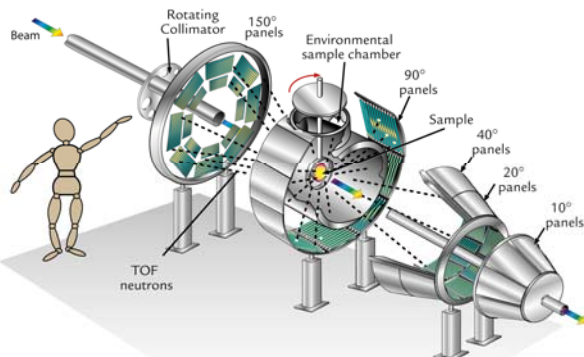
Abstract

We re-investigated the TTT diagram of U-10 wt.% Mo using isothermal high temperature neutron diffraction between 420°C and 560°C. U-10 wt.% Mo foils are fuel for the GTRI Reactor Convert program. Samples were ~250µm thick U-10Mo fuel foils with Zr cladding of 25µm on each side. Decomposition and ordering are competing processes, therefore, both α -U and an ordered γ -related phase γ' occur. Neutron diffraction uniquely allows identification of the involved phases and provides weight fractions as well as lattice parameters, crystal structures and textures as a function of holding time. From the lattice parameters, the Mo concentration in the residual γ -phase was estimated, showing enrichment in Mo. The texture showed a preference of the decomposition for specific crystal orientations, resulting in a substantial preferred orientation in both α -U and γ' .

Neutron diffraction proved to be a valuable tool to obtain a complete picture of such processes, without the deficiencies of classical methods such as DSC (not phase sensitive), dilatometry (sensitive to length changes due to transformation as well as Mo re-partitioning), metallography or X-ray diffraction (surface sensitive).

Introduction & Motivation: Stability of γ phase in U-10 wt.% Mo

- Global Threat Reduction Initiative (GTRI) of the National Nuclear Security Administration (NNSA, US DOE). Reduce and protect vulnerable nuclear and radiological material located at civilian sites worldwide by providing support for countries' own national programs.
- GTRI Reactor Convert program: Convert research reactors from the use of highly enriched uranium (HEU) to low enriched uranium (LEU).
- Baseline fuel for conversion of high performance research reactors: **Monolithic uranium-10wt.% molybdenum** (U10Mo, 0.25mm), encased in an aluminum cladding.
- γ phase (bcc) is preferred for the fuel application, stable in U10Mo above ~560°C, meta-stable at RT.
- Holding at temperatures below 560°C: Transforms from γ to α and γ' (U₂Mo, thermodynamically stable phases) with metastable ordered bcc phases γ' and γ'' also occurring.
- Fuel fabrication technique utilizes currently hot isostatic pressing (HIP'ing)
 - Aluminum cladding is HIP'ed to bond to the rolled U10Mo foil
 - Final crystal structure/phase composition of the U10Mo foil depends on the HIP'ing temperature profile



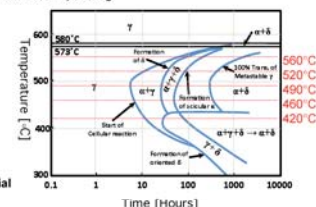
The HIPPO neutron time-of-flight diffractometer used in this study.
Wenk et al., NIM, 515 (2003) 575; Vogel et al., Powder Diffraction, 19 (2004) 65.

Neutron Diffraction to re-investigate the TTT diagram of U-10Mo

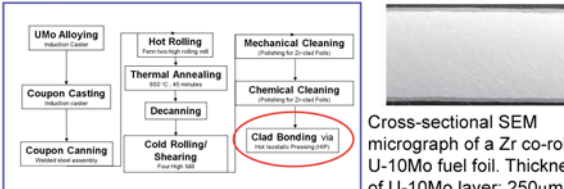
Previous investigations ex situ or using phase insensitive techniques, e.g.

- Halteman 1956 – XRD, metallography, density
- Repas et al. 1964 – metallography, dilatometry, microhardness, and XRD
- Kim et al. 1997 – SEM (EDS), DSC, XRD
- Seong et al. 2000 – ND (ex situ)
- Sinha et al. 2010 – XRD, metallography
- Burkes et al. 2010 – XRD, DSC, dilatometry
- Hengstler et al. 2010 – XRD, DSC, metallography

- XRD: Penetration depth few µm, ND: cm
- Dilatometry/DSC: not phase sensitive
- Here: Experimental setup to investigate material in situ during holding at HIP'ing temperature



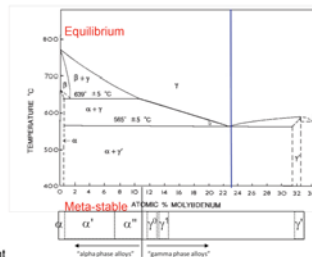
Monolithic Fuel Plate Fabrication Process: HIP'ing is crucial step



Moore & Marshall, "Co-Rolled U10Mo/Zirconium-Barrier-Layer Monolithic Fuel Foil Fabrication Process", INL/EXT-10-17774, 2010

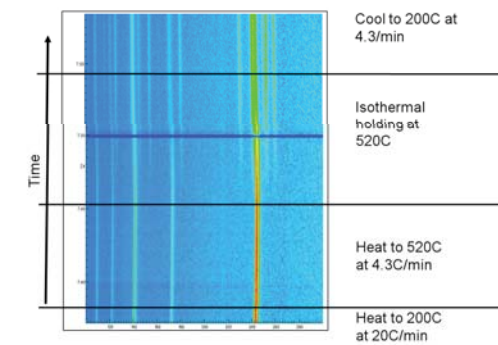
U-Mo Phase Diagram

- Both ordering and decomposition lower the free energy
- Ordering process is much faster
 - ⇒ intermediate ordered phases (may retard decomposition)
- Structures very similar to original γ /bcc structure
 - ⇒ diffraction pattern also very similar
 - ⇒ difficult to distinguish
 - ⇒ Some non-cubic
 - ⇒ Anisotropy!



Test Case: U-7Mo

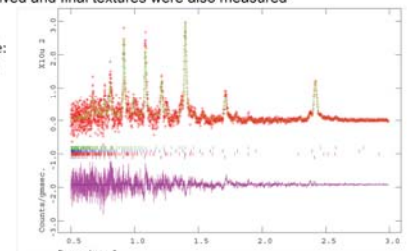
- 1 Minute count times, simulation of HIP treatment



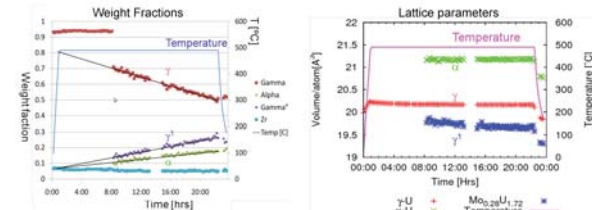
Experiment & Data Analysis

- Investigated 5 U-10Mo samples (Zr clad) at 420, 460, 490, 520, and 560°C
- Ramp rate was 8.3 degree/minute, same as during processing
- Data was acquired within 60 seconds integration time
- 10 patterns were combined to improve statistics for initial analysis
- Rietveld analysis of ~100 patterns per run (~15 hrs)
- As received and final textures were also measured

Example:
Last run
490C
 α -Zr
 γ' -U
 α -U
 γ -U



Results



- Decomposition into γ' (ordered phase) and α (very small solubility for Mo)
- Weight fractions (kinetics) consistent with diffusion-controlled process
- Lattice parameters for γ & γ' change during isothermal holding (Mo repartitioning)
- Lattice parameters for α remains constant (very little Mo solubility)
- Dilatometry would show length changes due to decomposition into two phases and Mo repartitioning ⇒ Neutron diffraction provides much more complete picture
- Lattice parameter of residual γ allows to estimate Mo concentration increases from ~9.95 wt.% to ~10.8 wt.%
 - Sinha et al., J. Alloys and Compounds 491 (2010) 753.
- Texture (not shown here) shows orientation preference for decomposition

Conclusions

- The TTT diagram of U-10Mo was reinvestigated
- Neutron diffraction is an efficient and reliable method to establish TTT diagrams.
- Circumvents deficiencies of XRD (surface), dilatometry (Δl is convolution of phase change and Mo repartitioning), DSC (not phase sensitive), and metallography (surface)
- Small samples (250µm foils) sufficient for modern neutron powder diffractometers



Radioparagenesis: Robust nuclear waste form design and novel material discovery

B. Dorado, MST-8; C. Jiang, Central South University, China; K. Sickafus, MST-8; B. Scott, MPA-MC; M. Nortier, C-IIAC; M. Fassbender, C-IIAC; L. Wolfsberg, C-IIAC; B. Uberuaga, MST-8; C. Stanek, MST-8



Summary

There is a renewed call for innovative options for nuclear waste management.

Secretary Chu recognized the importance of solving this problem during his confirmation hearing: "there's a lot of new science coming to the fore" ... "I pledge to use the best possible scientific analysis to figure out a way that we can go forward on nuclear disposal."

Nuclear waste disposal is the ultimate multiscale problem – from nanometers to kilometers, and picoseconds to millennia.

This project represents the science at the fore and aims to design robust nuclear waste forms.

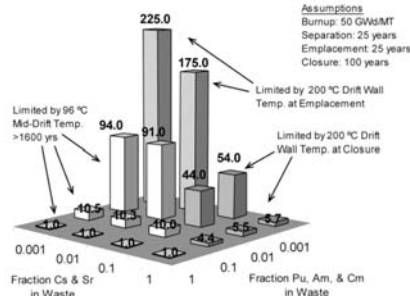


Figure 1: Prediction of the dependence of volumetric load decrease on a geologic repository on the fraction of short-lived fission products Cs and Sr, and radiotoxic actinides, from R.A. Wigeland, et al. Nuclear Technology 154 (2006) 95.

Reprocessing ("is an option" – S. Chu) allows for :

- * Significant radiotoxicity and volume minimization
- * Opportunity to consider customized waste forms for specific fission products.

Currently impossible to reliably predict the long-term performance of any waste form, e.g. glass is unstable.

Approach: combine recent studies of radiation tolerance and leaching resistance with predictions of long-term stability. Long-term stability insights are gained from a new field of study: **radioparagenesis**.

Radioparagenesis

"Paragenesis" is a geochemistry term meaning: the co-occurrence of different minerals, especially as a characteristic of their formation.

Whereas, we have introduced the term **radioparagenesis**, and define it as: *the formation of unconventional crystal structures for compounds formed during the chemical transmutation that occurs during radioactive decay.*

We have demonstrated the formation of radioparagenetic phases for a model waste form system – CsCl, where all Cs is the short-lived (30 year half-life) ^{137}Cs isotope.

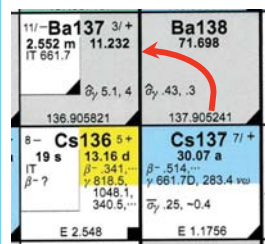


Figure 2: Decay chain of Cs-137 to Ba-137m, with a half-life of 30 years.

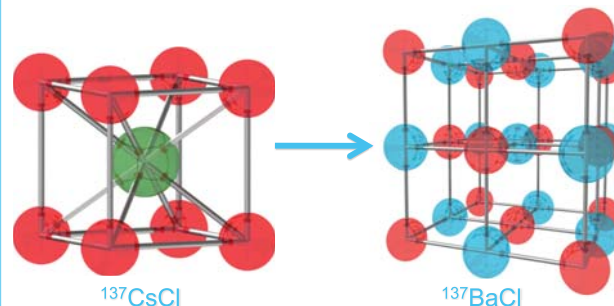


Figure 3: Formation of heretofore unobserved BaCl due to the decay of Cs-137.

According to classical ionic bonding arguments, one would expect BaCl_2 and not BaCl.

Verification of radioparagenesis

Experiments: use of ^{109}Cd synthesized at IPF at LANSCE

- Daughter product (Ag) is sufficiently chemically different
- Half-life of 461 days
- No recoil damage from the decay
- Characterization of a **small, highly radioactive CdS** sample performed in CMR hot cells

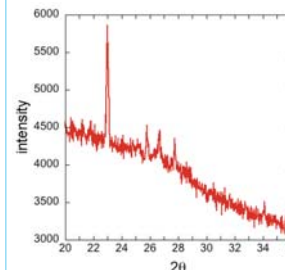
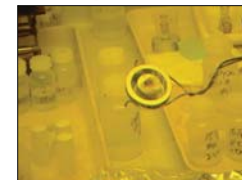


Figure 4: Experimental X-ray diffraction pattern obtained after one half-life of ^{109}Cd

Electronic structure calculations are used to identify (meta)stable phases of $\text{Cd}_{0.5}\text{Ag}_{0.5}\text{S}$

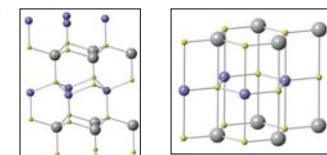


Figure 5: The two metastable phases of $\text{Cd}_{0.5}\text{Ag}_{0.5}\text{S}$

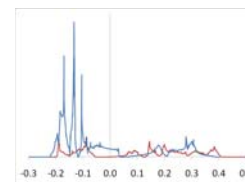


Figure 6: CdS (red) and AgS (blue) density of states

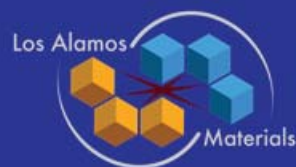
First principles predict RS-AgS to be metallic → **major change in the electronic structure due to radioactive decay**

Conclusion

- Hint of AgS as a **radioparagenetic phase**
- Significant changes in electronic structure (insulator vs metal)

Waste Forms? The implications of radioparagenesis are significant.

New Materials? Radioparagenesis may be a route for the synthesis of compounds not possible to form via conventional processes.



Fissionable Scintillators for Measuring Neutron Flux

S. Stange, N-2; E.I. Esch, N-1; R.E. Del Sesto, MPA-MC; R.E. Muenchausen, MST-7; F.L. Taw, C-IIAC;
F. Tovesson, LANSCE-NS; E.A. Burgett Idaho State University



Abstract

Fission chambers, ionization chambers containing one or more foils thinly coated with a fissile or fissionable material, are commonly used to measure neutron flux for nuclear physics experiments, such as those performed at the Los Alamos Neutron Science Center (LANSCE). These detectors are easy to operate, are not damaged by radiation, and have an acceptable efficiency for many applications. However, they also are prone to pulse pile-up, require long measurement times, and are bulky and fragile.

We proposed to address these issues by developing a nanocomposite fission detector, consisting of nanoparticles of fissionable material dispersed in a scintillating matrix. This would produce a detector that can be loaded with up to two orders of magnitude more uranium and has a pulse rise time that is two orders of magnitude faster. In addition, the use of a plastic matrix would make the detector far more robust than current fission chambers.

Figure 1. Two fission chambers used at LANSCE. The yellow foil visible in the opened chamber is coated with ^{235}U .



Material Selection

A suitable isotope for use in a fissionable scintillator must possess an appropriate fission cross-section, not interfere with the luminescence of the matrix material, and have an established path for nanoparticle synthesis. ^{232}Th was selected as a candidate isotope, and $\text{Th}(\text{NO}_3)_4(\text{TBP})_2$ was synthesized and loaded into a liquid scintillating matrix.

Optical Characterization

The optical properties and radiation response of the thorium-loaded scintillator were characterized using photoluminescence, radioluminescence, and ultraviolet-visible spectroscopy.

As shown in Figures 3 and 4, the addition of the thorium complex did not affect the emission wavelength or absorption edge of the liquid scintillator. The intensity of the emission increased by 4% due to the higher effective atomic number. A slight increase in transmission was also observed, due to index matching.

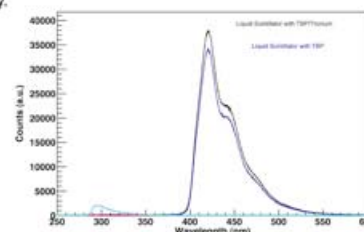


Figure 3. Radioluminescence (RL) of liquid scintillator loaded with thorium complex, compared with RL of liquid scintillator alone

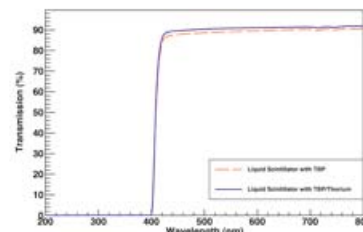


Figure 4. Comparison between the ultraviolet-visible spectroscopy of thorium-loaded and unloaded scintillators.

Beam Line Measurements

To evaluate the ability of the thorium-loaded detector to measure neutron flux, it was placed in the 90L beam line at LANSCE. Its measured spectrum contained events resulting from spallation neutrons and gamma-rays and alpha-particles produced by the decay of ^{232}Th . A second liquid scintillator, loaded only with the ligand (TBP) used in the thorium complex, was also characterized in the beam line as a baseline sample.



Figure 5. Thorium-loaded scintillator in the 90L flightpath at LANSCE.

Analysis of Beam Line Data

The time-of-flight spectra of the thorium-loaded and unloaded scintillators, shown in Figure 6, exhibited a sharp peak due to gamma-rays from the spallation gamma-flash (shown at $t=0$ in Figure 6) followed by a broad feature resulting from neutron events. The thorium-loaded detector also displayed a constant background resulting from ^{232}Th alpha-particle decays.

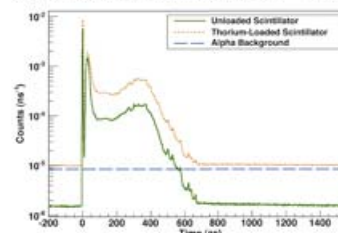


Figure 6. Time-of-flight spectra of unloaded and thorium-loaded scintillators.

Figure 7. Energy spectra following removal of alpha-particle background.

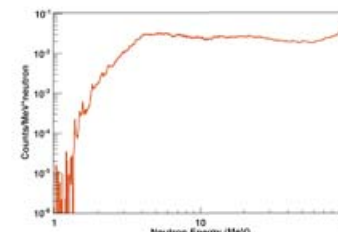
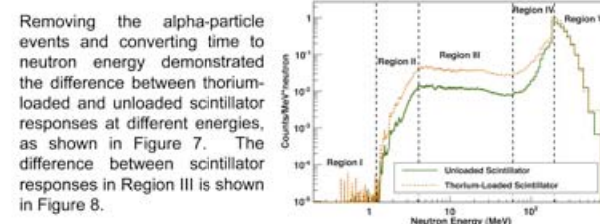
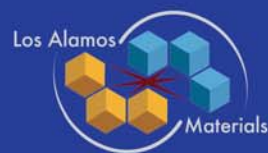


Figure 8. Difference in counts between thorium-loaded and unloaded scintillators.

Conclusions

The thorium-loaded scintillator tested in the beam line at LANSCE detected more events than an unloaded scintillator. The source of this increased count rate could not be definitively identified. Determining whether these events can be attributed to fission would require a digitizer with sufficient bits to allow for pulse-shape discrimination.



Colloidal nanomaterials for light harvesting applications

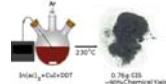
A. Pandey, L. Li, B.P. Khanal, H. Tsai, H. Wang, J.M. Pietryga, V.I. Klimov, C-PCS



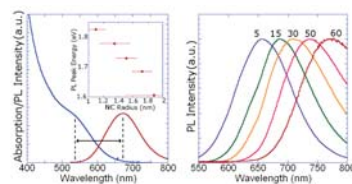
Photovoltaic applications stand to benefit significantly from the development of cheaper, more efficient materials. This requires progress in both chemical and physical principles of materials fabrication. In this poster we describe the synthesis and optical study of two different classes of nanoparticles:

- We demonstrate a novel waste free synthesis of copper indium sulfide (CIS) nanocrystals (NCs) and study their optical properties to determine the role of defects in this material.
- We also describe the synthesis of spectrally tunable metal-semiconductor hybrid structures that are potentially useful for several light harvesting and emission applications, and study their optical properties.

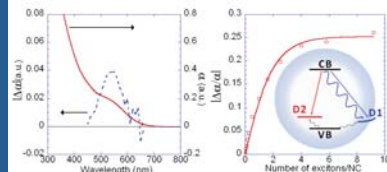
CIS NCs: Synthesis and spectroscopy



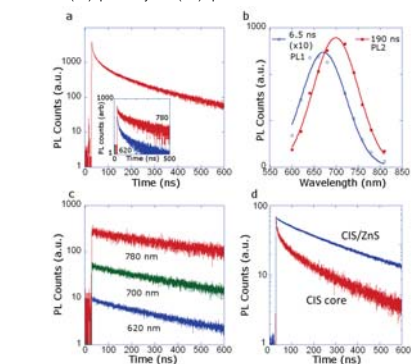
We synthesize CIS nanocrystals using a relatively waste free approach using the anion precursor, dodecanethiol (DDT) as a solvent, precursor and surfactant. The resultant crystals have an excellent size dispersion and photoluminescence (PL) quantum yields (QY) upto 10%.



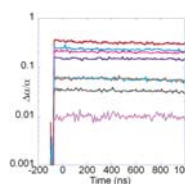
The resultant nanocrystals exhibit size tunable PL and absorption. Size control is achieved by increasing reaction times (indicated by the numbers in the right panel).



The Transient Absorption spectrum ($\Delta\alpha$ is the pump-induced change in the absorption coefficient α) of a typical CIS/CdS sample shows a bleach feature which is interpreted to arise from the filling of adobly degenerate level. The two recombination pathways observed in CIS NCs involve an electron in the quantized conduction band state (CB) and a hole trapped at either a surface defect (D1, blue) or an internal defect (D2, red). In CIS core/shells, D1 is suppressed, and overall relaxation becomes dominated by the slower D2-based channel.



Spectrally integrated PL decay for CIS NCs is biexponential with constants 7 ns and 190 ns that dominate emission decay on the blue and the red sides of the PL band, respectively (Panel a and inset). (b) Based on a double exponential analysis, the PL spectrum can be decomposed into a fast (open blue circles) and a slow (solid red squares) component centered at 670 and 700 nm, respectively. (c) Overcoating the core with a CdS layer eliminates the fast decay channel and results in spectrally uniform single-exponential decay with a 500 ns time constant. The overcoated materials exhibit quantum yields approaching 90% (d) Overcoating with ZnS also greatly reduces the contribution from the fast decay channel.

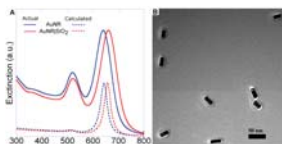


CIS based core/shell structures show suppressed Auger recombination on a nanosecond timescale. These materials could thus have significant applications in high performance LEDs and nanocrystal based lasers.

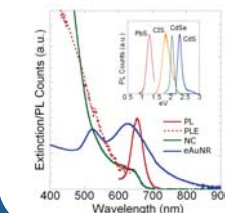
Li, L. et al. *J. Am. Chem. Soc.* 2011, 133, 1176.

General synthesis of metal-semiconductor hybrid superstructures

Electrons in metals may be forced into harmonic oscillations by an applied time varying electric field. These oscillations strongly interact with and modify optical fields in their vicinity. Metallic nanostructures can thus modify the behavior of proximal emitters and absorbers, by enhancing or suppressing coupling to radiation, or even enhancing the coupling between specific emitters



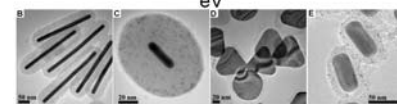
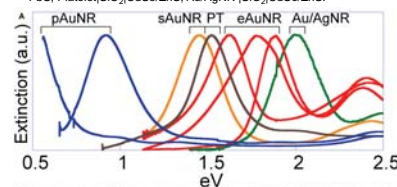
The silica layer is grown by hydrolysis of tetraethyl orthosilicate. Reaction progress is monitored by tracking the longitudinal plasmon as it shifts toward longer wavelengths. The dielectric constant of the shell is estimated to be ~ 2.09 . This suggests that silica shell is moderately porous, with $\sim 10-15\%$ of its volume being solvent accessible.



NCs may be attached to the Au/SiO₂ structures after amine functionalization. NC excitonic position may be tuned by varying either the size or the material. We have successfully used core-shell structures based on CdS, CdSe, CIS, PbS and PbSe, enabling the preparation of superstructures where the excitonic component may be tuned from the UV to the mid-IR. Shown here are the spectra of a CdSe based quantum dot tethered to a resonant AuNR.

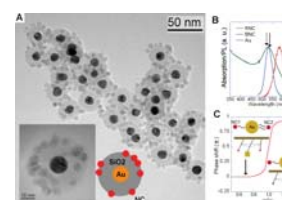


By using different plasmonic structures, it is possible to span UV to Mid-Infrared wavelengths. TEM images of various superstructures: (B)-(D) Pentahedral AuNR/SiO₂/CdSe/ZnS, Single crystal AuNR/SiO₂/PbS, Platelet/SiO₂/CdSe/ZnS, Au/AgNR/SiO₂/CdSe/ZnS.



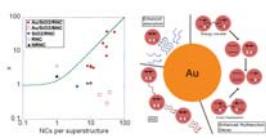
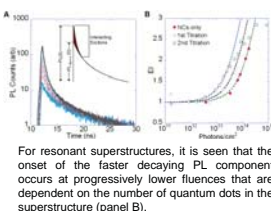
Khanal et al., in preparation.

Enhanced exciton-exciton interactions



The absorption spectrum of a sample of silica coated gold spheres, and the PL spectra of two different samples of NCs considered in this study are shown in panel B. The (dashed) solid arrows denote the (absorption) scattering maxima at the peak position. (C) The behavior of the two sets of NCs may be understood using the analogy of a set of oscillators coupled to a resonator.

Multi-exciton effects were studied in these structures by varying the excitation fluence at 400 nm, and observing photoluminescence (PL) decay dynamics as a function of power. The faster component in PL decay represents the onset of multi-exciton interactions in a subset of the ensemble. For free NCs in solution this effect is related to the cross sections of individual quantum dots.

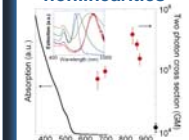


This effect is observed only in superstructures containing resonantly coupled NCs and is absent in NCs loaded onto silica spheres, as well as nonresonantly coupled NCs. Different phenomena may be invoked to explain these observations including enhanced absorption, plasmon mediated "spasing," enhanced nonradiative decay, etc. We argue that none of the above effects can account for the observed phenomena on basis of the saturation behavior of this material system.

These results are indicative of strong inter-exciton interactions in these systems, that do not significantly effect final quantum yields.

Pandey et al., in preparation.

Plasmon enhanced nonlinearities



The coupling of NCs to an AuNR has a very significant effect on the two photon cross sections with the values measured at 800nm being greatly enhanced relative to the already large value of the original bare NCs. In testament to the importance of fine-tuning, this enhancement increases from 5- to 30-fold as the AuNR plasmon is tuned over the excitation wavelength, reaching as high as 4×10^5 GM, by far the highest values ever reported.

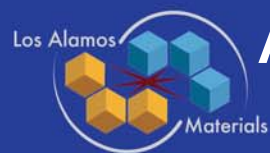
Conclusions:

We developed and studied different examples of nanomaterials with functionalities relevant to light harvesting and emission applications. CIS NCs are a promising alternative to II-VI and IV-VI materials that suffer from numerous problems including toxicity. Metal-semiconductor hybrid superstructures with resonances that span the optical spectrum starting from the ultraviolet to the mid-infrared were synthesized and studied as part of a separate study. These materials exhibit novel optical properties including enhanced interaction with radiation as well as enhanced inter-emitter interactions. These novel materials will benefit a broad range of light harvesting and emission applications.

Acknowledgements:

This work was performed at the Center for Advanced Solar Photophysics, an EFRC. A. P. and B. K. were supported by Los Alamos Director's Fellowships.





A comparative study of carrier multiplication yields in PbSe and PbS nanocrystals

J. Stewart, C-PCS; A. Midgett, NREL, CU; L. Padilha, C-PCS; D. Smith, NREL; J. Pietryga, C-PCS;
J. Luther, M. Beard, NREL; A. Nozik, NREL, CU; and V. Klimov, C-PCS

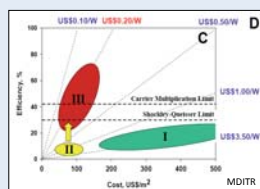


Abstract

• Current solar cell technology (1st gen.) relies on very expensive “pure” bulk materials and their efficiencies are limited to the S-Q limit. For these reasons, 1st gen. solar cells are not likely be competitive with burning fossil fuels.

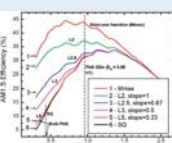
• Semiconductor nanocrystals (3rd gen.) are much cheaper (solution processable) while having comparable or higher efficiencies.

• The work here aims to discern which bulk properties or phenomena determine the efficiency of nanocrystals



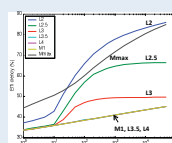
Carrier multiplication

Efficiency predictions



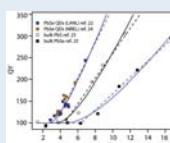
- More efficient carrier multiplication leads to dramatically more efficient solar cells
- Optimal range of bandgaps is much larger and trends to the IR

Max eff. vs concentration



- Carrier multiplication devices are predicted to benefit strongly from solar concentration

Bulk vs. nanocrystals



- Nanocrystals are indeed more efficient than bulk!

Comparing PbSe and PbS

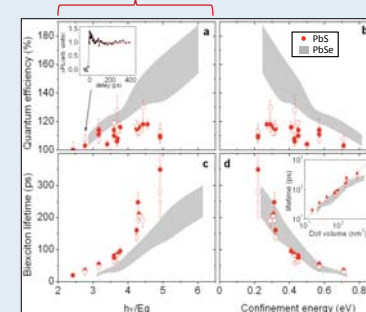
PbSe and PbS are both IR band gap materials, have large Bohr exciton radii, and abundant

Element	Abundance
Pb	0.0001%
Se	0.0001%
S	0.0001%
Te	0.0001%
Bi	0.0001%
As	0.0001%
Ge	0.0001%
Si	0.0001%
Al	0.0001%
Fe	0.0001%
Cu	0.0001%
Ag	0.0001%
Au	0.0001%
Co	0.0001%
Ni	0.0001%
Zn	0.0001%
Ca	0.0001%
Mg	0.0001%
Ba	0.0001%
La	0.0001%
Ce	0.0001%
Pr	0.0001%
Nd	0.0001%
Pm	0.0001%
Sm	0.0001%
Eu	0.0001%
Gd	0.0001%
Tb	0.0001%
Dy	0.0001%
Ho	0.0001%
Er	0.0001%
Tm	0.0001%
Yb	0.0001%
Lu	0.0001%

PbSe	PbS
Bulk band gap	0.27eV
LO phonon energy	17meV
$\epsilon(0)$, $\epsilon(\infty)$	210, 23
Effective mass	0.04
$\hbar\omega_{LO}$	66meV
Lattice structure	Cubic

PbS	PbSe
Bulk band gap	0.42eV
LO phonon energy	28meV
$\epsilon(0)$, $\epsilon(\infty)$	168, 17
Effective mass	0.08
$\hbar\omega_{LO}$	24meV
Lattice structure	Cubic

Both PbSe and PbS have a low threshold for CM

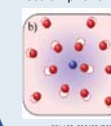


Unexpectedly, we observe striking differences in CM yields despite their similarity in bulk semiconductors

Similar biexciton lifetimes suggest similar Coulomb interaction strengths... CM yields should be similar

How do phonon emission rates compare?

Electron-phonon interactions are described within the polaron framework



PbSe	PbS
$\alpha_p = 0.22$	$\alpha_p = 0.33$
$\hbar\omega_{LO} = 17meV$	$\hbar\omega_{LO} = 28meV$

Phonon emission rates should be higher in PbS than PbSe

Conclusions

- We synthesize very high quality PbSe and PbS nanocrystals and compare carrier multiplication yields and biexciton lifetimes.
- PbSe and PbS are nearly ideal for comparison due to their similar bulk properties.
- Despite very similar biexciton lifetimes, we observe strikingly different CM yields.
- Phonon emission rates derived within the polaron framework are consistent with PbS having stronger phonon emission rates as compared to PbSe

J. T. Stewart *et al.*, “A comparative study of carrier multiplication yields and biexciton lifetimes in PbS and PbSe nanocrystals.” In preparation for *Nano Lett.*

Nanocrystal properties

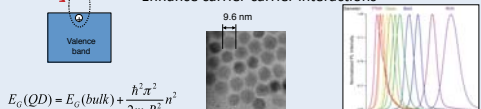
Chemistry (synthesis)



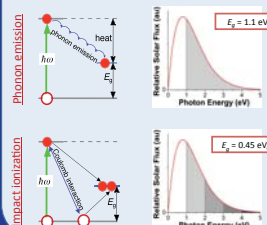
- Low temperature colloidal chemistry (cheap)
- Easily scalable
- Spin-coating, ink-jet printing ...
- Abundant materials (Si, Ge, PbSe, PbS ...)
- Reproducible synthesis
- All chemistry done “in house”

Physics (control optical properties with size)

- NC size (few nm) << Bohr exciton radius (10s of nm)
- Quantum confined system
- Enhance carrier-carrier interactions



Hot exciton cooling

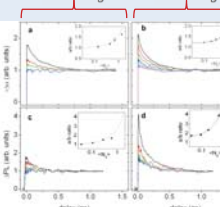


- Single photon = 1 e-h pair
- Excess energy is lost in heat
- Phonon emission is the dominant decay mechanism in bulk

- Single photon > 1 e-h pair
- Excess energy is converted into more excitons
- Impact ionization may be more efficient in nanocrystals

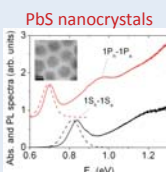
Ultrafast spectroscopy

$\hbar\omega < 2E_g$ $\hbar\omega > 2E_g$



Transient Absorption

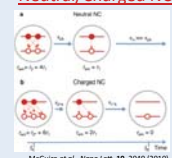
Up-converted Photoluminescence



$I_t = I_0 e^{-\alpha d}$

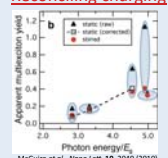
Effects of photocharging

Neutral/Charged NC



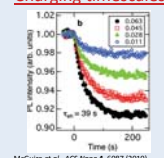
- Photoexcitation can lead to photocharging (a trapped charge)

Reconciling charging



- Previous discrepancies in reported CM yields were caused by photocharging

Charging timescales



- Charging occurs on very slow timescales. Stirring the sample vigorously refreshes sample continuously





Assessment of silicon nanowire architecture for PV application

S. Dayeh, M J. Yoo, D. Perea, MPA-CINT; I. Campbell; MPA-11;
S. Picraux, MPA-CINT

I-Introduction

• 1D semiconductor nanowire arrays have a great potential for improved photovoltaic performance and cost reduction over their bulk counterparts with sufficiently thin absorption lengths. This is due to (i) improved absorption from diffuse light scattering in nanowire arrays, (ii) short collection lengths of minority carriers that are radially separated and collected normal to the light absorption direction, (iii) flexibility of integration on a variety of carrier substrates.

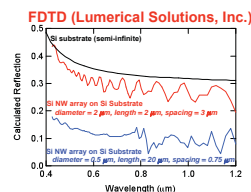
• The goals of this project are to experimentally determine whether silicon nanowire solar cells can achieve performance close to that of crystalline silicon cells but with the much lower costs of thin film, amorphous Si solar cells. This is being accomplished by:

- Providing more complete device physics models for assessing radial nanowire solar cells.
- Fabrication of metal-catalyst free Si nanowire pillar arrays in a Fab-compatible process followed by epitaxial growth of doped shells.
- Fabrication of nanowire arrays on stainless steel substrates.
- Experimentally probe Si nanowire solar cell performance, measure their minority carrier lifetimes and diffusion lengths, minimize device parasitics such as access and contact resistances, and feedback these for improving solar cell design & performance.

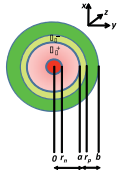
II-Modeling, Simulation, & Projected Performance/Cost

• While there are initial reports on modeling radial nanowire solar cells, intuitive, simple and more complete modeling of nanowire solar cell performance is yet to be demonstrated.

• For example, the first design parameters one cares about in designing nanowire solar cells are optimal array geometric figures (such as diameter, length, and pitch) that are then coupled to required doping densities and appropriate p- and n-layer thicknesses. We perform the first using Finite Difference Time Domain methods and the second through self consistent solutions to Poisson-Continuity equations.



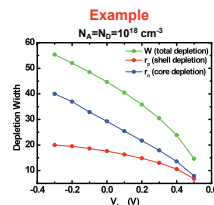
Characteristic equation for determining depletion region widths



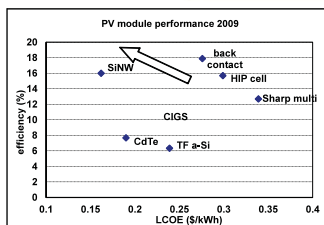
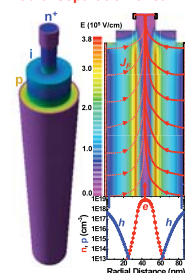
$$\frac{2\epsilon_s V_{bi}}{qa^2} = \frac{N_A^-}{2} \left(\frac{r_p}{a} \right)^2 \ln \left(\frac{\left(\frac{r_p}{a} \right)^2}{\frac{N_A^- + N_D^+}{N_D^+} - \frac{N_A^-}{N_D^+} \left(\frac{r_p}{a} \right)^2} \right) + \frac{1}{2} (N_A^- + N_D^+) \ln \left(\frac{N_A^- + N_D^+}{N_D^+} - \frac{N_A^-}{N_D^+} \left(\frac{r_p}{a} \right)^2 \right)$$

If $N_A^- = N_D^+ = N \rightarrow$

$$\frac{2\epsilon_s V_{bi}}{Na^2} = \frac{1}{2} \left(\frac{r_p}{a} \right)^2 \ln \left(\frac{\left(\frac{r_p}{a} \right)^2}{2 - \left(\frac{r_p}{a} \right)^2} \right) + \ln \left(2 - \left(\frac{r_p}{a} \right)^2 \right)$$



Radial separation of carriers



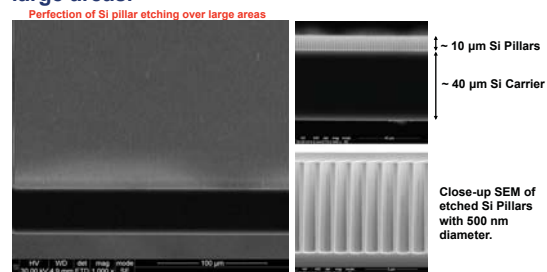
Levelized Cost of Electricity (LCOE) Based on NREL-LCOE calculator

Module	Cell type	Efficiency (%)	Array power (kW)	Installed cost (\$/W)	LCOE (\$/kWh)
SunPower SPR-220	back contact monocrystalline Si	17.88%	7.345	\$6.44	\$0.276
Sanyo HIP-190DA1	monocrystalline Si	15.58%	7.419	\$9.49	\$0.299
Sharp 165U1	multicrystalline Si	12.69%	6.932	\$10.76	\$0.339
Unisolar US64	thin film amorphous Si	6.33%	7.042	\$8.00	\$0.239
Si-NW module	radial junction Si nanowire	16%	7.286	\$4.45	\$0.162

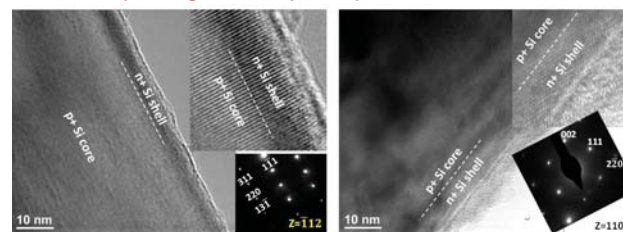
Module performance and cost provided by EERE partners David Evans, Paul Schuele, Sharp Labs

III-Fabrication, Growth and Characterization

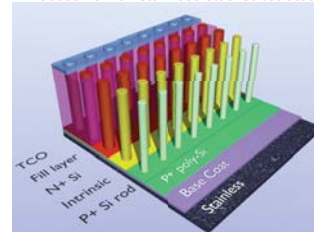
• BOSH deep Inductive Coupled Plasma (ICP) etching is used to etch Si nanowire pillars over large areas.



Si epi-shell growth on top-down processed nanowires



Process flow on stainless steel substrates

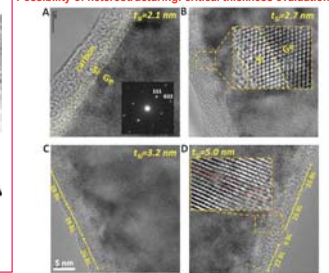


Exfoliation of thin SS



First experimental measurement of critical thickness in lattice mismatched semiconductor nanowires and first observation of defect types that arise from such mis-match.

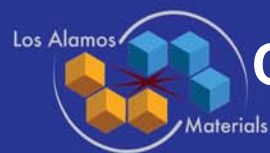
Possibility of heterostructuring: critical thickness evaluation



IV-Summary

- Modeled absorption and currently developing transport modeling for Si radial nanowire solar cells.
- Established top-down and bottom up processing of Si nanowires on various substrates.
- Implemented epi-growth of crystalline doped shells on top-down processed nanowires.
- Determined critical thickness and dislocation loop types in Ge/Si core/shell nanowire heterostructures.
- Electrical/optical characterization on Si radial nanowire solar cells are currently in progress.

We acknowledge funding from LDRD & EERE.



Controlling electrode morphology to improve fuel cell performance and durability



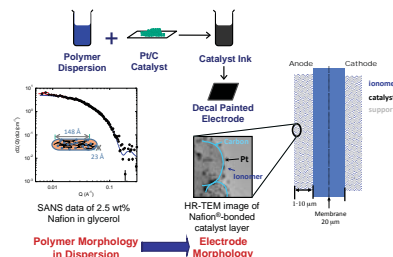
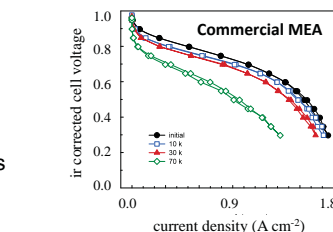
C. Welch, E.B. Orler, MST-7; R. Hjelm, LANSCE-LC; C. Johnston, Y.S. Kim, B. Choi, MPA-11;
A. Labouriau, MST-7; N. Mack, C-PCS; M. Hawley, MST-8; K. More, ORNL

The Problem

- Fuel cell performance declines as cell is cycled
- Partly caused by agglomeration of catalyst nanoparticles & subsequent loss in electrochemically active surface area (ECSA)
- Partly caused by unknown factors, which may be related to electrode morphology
- DOE has set a target of achieving less than 30 mV loss after 30k cycles
- Extensive efforts have been aimed at developing new catalysts
- Other contributions to the problem have largely been ignored

Our Approach

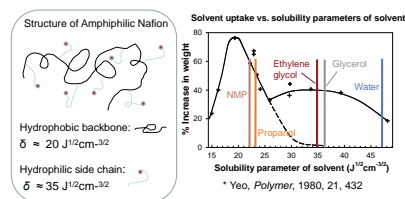
- Hypothesis: Morphology of Nafion dispersions affects electrode morphology and thus, cell performance
- Approach: Characterize Nafion dispersion morphology and relate to cell performance and durability
- Connecting the dots: Relationship between dispersion and film morphology



The Thermodynamics

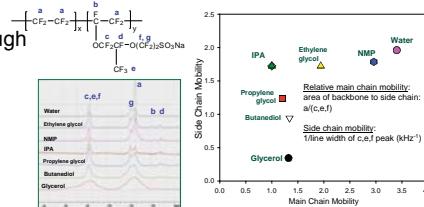
- Amphiphilic ionomer has dual solubility parameters
- Solvent interactions with both parts of ionomer can be used to control dispersion morphology
- Interactions are quantified with the Flory-Huggins parameter:

$$\chi = \frac{V_s}{RT} (\delta - \delta_s)^2 + \chi_{Entropy}$$



¹⁹F NMR of Dispersions

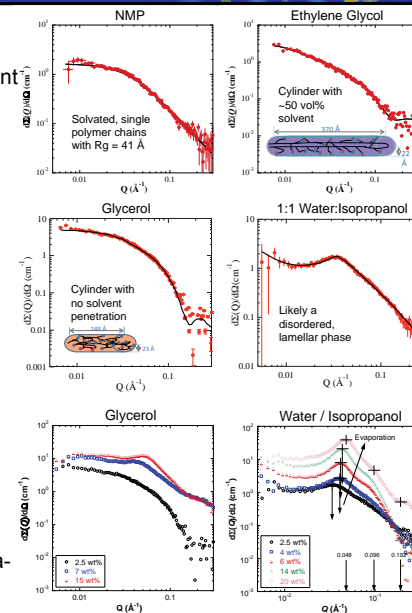
- Gives indication of polymer-solvent interactions through mobility measurements
- Glycerol: Poor solvent for both backbone & side chain
- Ethylene glycol: Good solvent for side chain; fair for backbone
- NMP: Good solvent for both backbone & side chain
- Water: Better solvent for side chain than backbone
- IPA: Better solvent for backbone than side chain



SANS of Dilute Dispersions

- Investigation of dilute dispersions in range of solvents yields insight into how polymer-solvent interactions control dispersion morphology

Solvent	Hoy δ (MPa ^{1/2})	χ_m	χ_p	Morphology
Glycerol	33.8	0.91	0.86	Dense cylinder
H ₂ O	47.9	6.4	1.7	Swollen lamellar
IPA	23.5	0.39	0.77	Swollen cylinder
Ethylene glycol	29.9	2.6	0.41	Swollen cylinder
NMP	23.1	0.72	0.41	Solvated chains

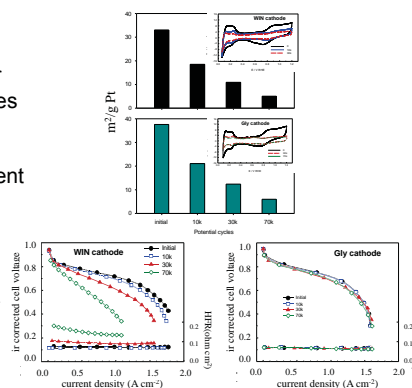


SANS of Evaporating Dispersions

- In glycerol, cylindrical particles pack and interconnect to form gel at 7 wt% as solvent evaporates
- In water / IPA, IPA evaporates preferentially
- Lamellar D-spacing decreases & order increases
- Gel that forms at 20 wt% shows strong ultra-low-Q scattering that suggests lamellar ordering at longer length scales, 2 – 3 μ m

Characterization of Electrode Films

- ECSA behavior as MEA is cycled is similar for both glycerol- and water/IPA-derived electrodes
- TEM analysis of Pt particles shows similar agglomeration behavior
- Yet, durability tests show dramatic improvement for glycerol-derived electrode



Summary

- Our work suggests that electrode morphology strongly influences fuel cell durability
- We can control electrode morphology through polymer-solvent interactions at play during electrode fabrication

Acknowledgments: LANSCE for SANS beam time; NIST for USANS beam time & Igor SANS analysis routines; Nancy Garland & DOE-EERE Fuel Cell Technologies program for financial support





Nanoscale ceramic catalyst support synthesis

E. Brosha, L. Elbaz, MPA-11; K. Blackmore, A. Burrell, MPA-MC; N. Henson, T-1



Abstract

Alternative supports for polymer electrolyte membrane fuel cells were synthesized and catalytic activity was explored using electrochemical analysis. High surface area, molybdenum nitride supports were synthesized by rapidly heating a gel of polyethyleneimine bound molybdenum in a tube furnace under a forming gas atmosphere. Subsequent disposition of platinum through an incipient wetness approach lead to dispersed crystallites of platinum on the conductive support. All the ceramic materials were characterized with XRD, SEM, TEM and electrochemical analysis. The supports without platinum are highly stable to acidic aqueous conditions and show no signs of oxygen reduction reactivity (ORR). However, once the 20 wt% platinum is added to the material, ORR activity comparable to XC72 based materials is observed.

Introduction

Catalyst support durability is currently a technical barrier for commercialization of polymer electrolyte membrane (PEM) fuel cells, especially for transportation applications. Degradation and corrosion of the conventional carbon supports leads to losses in active catalyst surface area and, consequently, reduced performance. As a result, the major aim of this work is to develop potential support materials that target the principal shortcomings of present-day PVC catalysts by improving Pt-support interaction, yet sustain bulk-like catalytic activities with very highly dispersed particles. This latter aspect is key to attaining the 2015 DOE technical targets for platinum group metal (PGM) loadings (0.20 mg/cm²). To avoid carbon degradation altogether, it has been proposed by numerous fuel cell research groups to replace carbon supports with conductive materials that are ceramic in nature. Intrinsically, these many conductive oxides, carbides, and nitrides possess the prerequisite or at least acceptable electronic conductivity required for electrochemical reactions, and offer corrosion resistance in PEMFC environments; however, most reports indicate that obtaining sufficient surface area remains a significant barrier to obtaining desirable fuel cell performance. Ceramic materials that exhibit high electrical conductivity and necessary stability under fuel cell conditions must also ideally exhibit high surface area as a necessary adjunct to obtaining high Pt dispersions and Pt utilization targets. Our goal in this work is to identify new synthesis approaches together with materials candidates that will lead to ceramic supports with high surface areas that are capable of serving as a host for high Pt dispersions.

Project Objectives

- Project Objective: Develop a ceramic alternative to carbon material supports for a polymer electrolyte fuel cell cathode.
- Ceramic support must:
 - have enhanced resistance to corrosion and Pt coalescence.
 - preserve positive attributes of carbon such as cost, surface area, and conductivity.
 - be compatible with present MEA architecture & preparation methods.
- Materials properties goals include:
 - high surface area & high Pt utilization
 - enhanced Pt-support interaction
 - adequate electronic conductivity
 - resistance to corrosion
 - synthesis method / procedure amenable to scale-up & reasonable synthesis costs

Focus on Select Support Candidate Materials

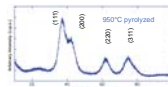
- Transition metal nitrides: Mo-N, Zr-N
 - Corrosion resistance, high electronic conductivity, catalytic properties
- Sub-stoichiometric titania (TiO_x)
 - Ti₂O₃ (Magnéli phase)
 - High electronic conductivity, refractory, stable in acid media.
 - Reports of strong metal-support interactions with noble metals.
 - Resistance to oxidation and demonstrated electro-catalytic activity for both hydrogen and oxygen / Pt.
 - TiO: conductive but not as high as Magnéli phase

Experimental Synthesis Methods

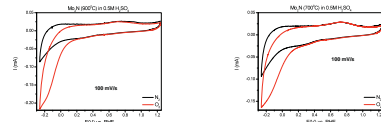
- Polymer assisted deposition (PAD) nitrides and sub-oxides of titania.
 - PAD precursor routes to produce ceramic materials with high surface area.
 - Corrosion resistance, high electronic conductivity, catalytic properties
- Sub-stoichiometric titania (TiO_x)
 - Ti₂O₃ (Magnéli phase)
 - High electronic conductivity, refractory, stable in acid media.
 - Reports of strong metal-support interactions with noble metals.
 - Resistance to oxidation and demonstrated electro-catalytic activity for both hydrogen and oxygen / Pt.
 - TiO: conductive but not as high as Magnéli phase
- Theory/Modeling support to aid experimental effort to provide data on stability of the support in absence of Pt particles and nature of Pt-support interactions
 - Surface/cluster models useful to predict effects of particle size reduction, conductivity.
 - Study nature of Pt binding sites, interaction energy, etc.

1st Year Results: A Mo₂N Front Runner

- Molybdenum Nitride Synthesis:
 - Mo₂N cubic phase.
 - XRD: average crystallites ca. 1 – 2nm.
 - 700 – 950°C pyrolysis T with 950°C optimum
- BET: 250 – 300m²/g typical surface areas
- Electronic conductivity (resistance)
 - 2-gt measurement, powder measured by compacted powder in 1/2" dia. fixture with uni-axial applied force.
 - Mo₂N (950°C): 3.3Ω
 - Vulcan XC-72R measured in same fixture: 1.8Ω
- ORNL TEM Analysis
 - < 2nm particle sizes with agglomerates of nano-particles, ~0.2µm to over 2µm
 - Highly crystalline structure consistent with cubic Mo₂N and nicely faceted

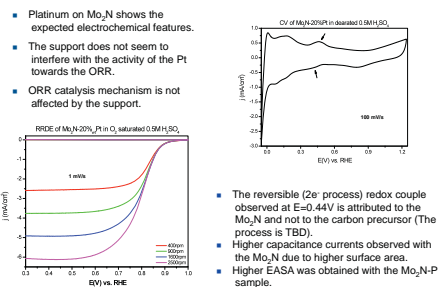


Mo₂N Stable Support and Shows Inactivity



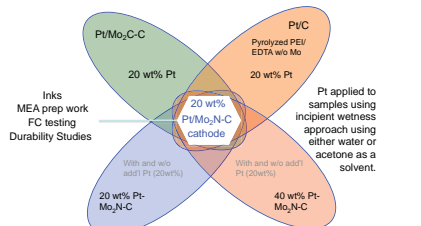
- The electrochemistry of the heat treated Mo₂N was studied in 0.5M H₂SO₄.
- The Mo₂N devoid of Pt catalyst shows no activity toward ORR.
- The support shows stability in acidic medium (no effect was observed while running multiple CV's with the support).

Pt/Mo₂N : ORR Activity Shown



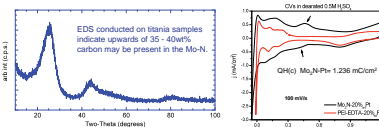
- The reversible (2e⁻ process) redox couple observed at E=0.44V is attributed to the Mo₂N and not to the carbon precursor (The process is TBD).
- Higher capacitance currents observed with the Mo₂N due to higher surface area.
- Higher EASA was obtained with the Mo₂N-Pt sample.

Electrochemical Studies Methodology

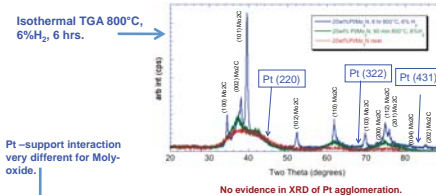


Source, Properties, and Influence of C Remnants

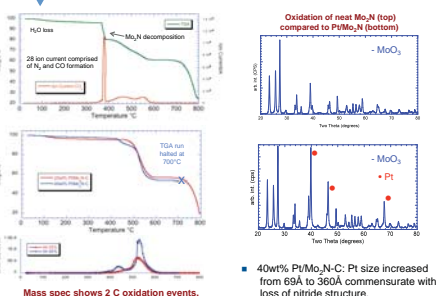
- Early EDAX measurements of Mo₂N suggested Carbon – confirmed with PAD TIO.
- Sample prepared without Mo source: PEI/EDTA pyrolyzed at 950°C; same procedure used for Mo₂N synthesis.
- BET surface area is low (over 100x lower) compared to Mo₂N; 1.7 m²/g
- Confirms broad peak at 25° in all XRD data is from the carbon remnants.
- Platinized carbon residue not a significant contributor to activity.



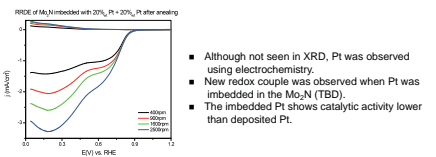
- Release of N₂ commensurate with decomposition of Mo₂N.
- Prolonged anneal ca. synthesis temperature fosters Mo₂C formation at the expense of Mo₂N.
- Residual carbon remains.



Pt-support interaction very different for Molybdenum.

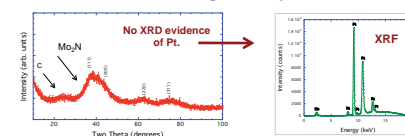


- 40wt% Pt/Mo₂N-C: Pt size increased from 69Å to 360Å commensurate with loss of nitride structure.
- Dramatic increase in Pt mobility once Mo₂N converts to MoO₃.



- Although not seen in XRD, Pt was observed using electrochemistry.
- New redox couple was observed when Pt was imbedded in the Mo₂N (TBD).
- The imbedded Pt shows catalytic activity lower than deposited Pt.

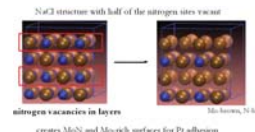
In situ Pt-Mo₂N Formation Using PAD Process Leads to Stable, Ultra-high Pt Dispersions



Computational Studies of Thin-Film Molybdenum Nitride Supports for Platinum Electrodes

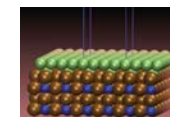
- Aims for FY11:
 - Focus on dominant γ-Mo₂N identified from characterization of samples
 - Construct structural models for phase – effect of non-stoichiometry and defect structures
 - Calculate binding energies for platinum mono-layers on surface models
 - Calculate trends in predicted over-potential for models
- Approach:
 - Calculations to be performed using plane wave periodic density functional theory calculations (VASP software)

A structural model of γ-Mo₂N



Platinum strongly bound to defective surface

- identify most favorable sites for single Pt atoms
- B (4-fold) > C (bridge) > A (on-top)
- and construct a monolayer based on these results



Mo-brown, N-blue, Pt-green

Collaborations / Distribution of Technical Personnel

- Materials characterization: XRD, XRF and thermal analysis; Eric Brosha (PI)
- Electrochemical characterization, ink and MEA prep; Lior Elbaz
- PAD synthesis, high surface area powder supports; Anthony Burrell and Karen Blackmore
- Support Modeling; Neil Henson
- Conductive aerosol derived supports; Timothy Ward and Rosalba Rincon
- XPS characterization; Kateryna Artushkova
- TEM Characterization; Karen More (PI – special materials)

Acknowledgments

We wish to thank Nancy Garland and the U.S. DOE Hydrogen Program for providing funding for this work.



Membrane Materials for Energy Applications



K.A. Berchtold, R.P. Singh, K.W. Dudeck, V.A. Kusuma, MPA-MC;
D. Yang, C. F. Welch, MST-7; B. Benicewicz, U. South Carolina; Y.C. Jean, UMKC

Introduction

Capturing carbon dioxide from mixed-gas streams is a first and critical step in carbon sequestration. To be technically and economically viable, a successful separation method must be applicable to industrially relevant gas streams at realistic temperatures, and be compatible with large gas volumes. While the separation of CO₂ from process streams is readily accomplished via standard separation techniques such as amine scrubbing and pressure-swing adsorption, the effectiveness of these current technologies for separating CO₂ is limited. These techniques require low temperatures and produce a low-pressure CO₂ stream, resulting in a significant energy penalty for separating CO₂. In contrast, polymer-based membrane separations are less energy intensive, requiring no phase change in the process, and typically provide low-maintenance operations. Polymer membranes have been used successfully in a number of industrial applications. However, successful use of a polymer membrane in a synthesis (syn) gas separation requires a membrane that is thermally, chemically, and mechanically stable at high temperature and high pressure in the presence of the chemically challenging syngas components. The commercially available polymeric materials currently employed in separation applications are not stable in these demanding environments to the degree required. Current membrane materials are often subject to chemical degradation by minor components in the process stream, a problem that is exacerbated by elevated temperature. Additionally, as the glass transition temperature of the polymer is approached, membrane selectivity is significantly reduced, and flux decline due to membrane compaction is increased. Consequently, there is a compelling need for membrane materials and subsequently capture systems based on those materials that can operate under more extreme environmental conditions for extended periods of time while providing a level of performance that is economically sustainable by the end user.

Separation and Capture

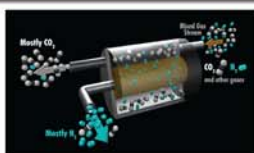
National Needs/Membrane Opportunities

- High Temperature Membranes are in Great Demand...
 - Membrane reactors, Synthesis gas separations (Power systems, IGCC, Gas-To-Liquids, Hydrogen production, Fuels & Chemicals Processing and Production)
 - Alternative technologies (PSA, TSA, adsorption, absorption, cryogenic) have drawbacks (Selextol-benchmark IGCC design)
 - Energy intensive
 - Produce CO₂ at atmospheric pressure
 - Low temperature processes
 - Can be high maintenance and cost (capital and operating) compared to membranes
- But are in Short Supply – Materials
 - Existing membrane materials have limiting temperatures, selectivity, productivity, chemical resistance, material properties

Polymeric membranes based on benzimidazole chemistries are being developed to address the aforementioned limitations of the current state of the art and the corresponding separations needs of the utility sector. Work to-date by our project teams indicates that the developed materials function at significantly higher temperatures (>>300°C) than current commercially available polymeric membranes (<150°C). In addition, the materials provide improved performance while exhibiting long-term temperature stability, sulfur tolerance, and overall durability over a broad range of industrially relevant operating conditions.

Focus: Solid Fuels Gasification

- Coal accounts for approximately half of the electricity generated in the US
 - 27% of the world's coal is in the US
- Coal produces a large percentage of the CO₂ emissions from power generation
 - Most challenging syngas stream
- IGCC with CO₂ capture using today's separation technologies and associated inefficiencies leads to a >25% in COE
 - ~75% of that cost is attributable to the energy consumption and losses associated with CO₂ capture/separation from the syngas stream
 - Over 50 IGCC projects totaling > 25,000 MW have been announced or are in the planning stages worldwide
- Technology developed also applicable to numerous other synthesis gas separations



Objective

Develop and demonstrate polymer-based membrane chemistries, morphologies, structures, deployment platforms, and sealing technologies that achieve the critical combination of high selectivity, high

permeability, chemical stability, and mechanical stability all at elevated temperatures (>150 °C) and packaged in a scalable, economically viable, high area density system amenable to incorporation into an IGCC or ammonia plant for pre-combustion CO₂ capture.

Membrane Basics

The permeability of each gas component through the membrane, P_i , is the product of the mobility (diffusivity) and solubility coefficients of penetrant i .

$$P_i = D_i S_i$$

As the separation temperature increases the solubility contribution to permeability becomes negligible. Thus, molecular sieving is the dominant separation mechanism in these materials.

Molecular Sieving



Primarily size based diffusion with some sorption effects

Free Volume Architecture Manipulation for Enhanced Gas Permselectivity

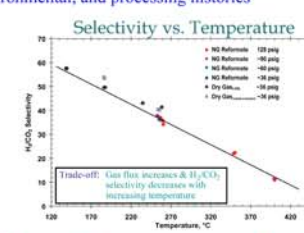
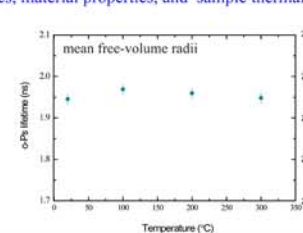
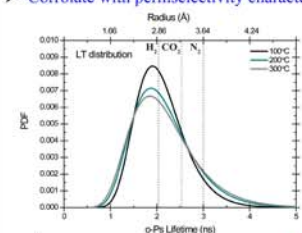
- Pre- and post-polymerization modifications are utilized to affect material properties and free-volume characteristics
 - Branching and crosslinking chemistries are utilized to manipulate and lock in network structures
 - Systematic main chain and molecular weight variations are introduced to chemically and physically manipulate free volume element character

Free volume estimated using Bondi group contribution method:

Polymer Group Abbreviation	m-PBI	p-PBI	4Br-PBI	2Br-PBI	5OH-PBI	6F-PBI	O-PBI	Cyclohexane-PBI	SO ₂ -PBI	Naphthalene-PBI
Structure of R										
FFV of PBI	0.131	0.117	0.125	0.125	0.160	0.186	0.141	0.114	0.177	0.145

Positron Annihilation Spectroscopy (PAS) provides experimental insight into free volume element sizes and distributions

- Depth profiles of thin film membrane materials are evaluated using Doppler Broadening Energy Spectroscopy (DBES) with positron incident energies from 0 to 30 keV. DBES is also utilized to evaluate influences of sample history
- Free volume characteristics are evaluated using lifetime measurements (PALS) both in the bulk and as a function of depth
- Correlate with permselectivity characteristics, material properties, and sample thermal, environmental, and processing histories



Approach

- Selective Layer Design Synthesis & Evaluation
 - Tailored PBI-based materials synthesis
 - Development of a fundamental understanding of how to manipulate and control the free-volume architecture and thus permselectivity of the selective layer
- Membrane Fabrication, Optimization, & Testing
 - Ultrasonic spray-coating technology (USCT) based fabrication development
 - Hollow fiber fabrication methodology development
 - Sealing materials & methods development
 - Evaluation in realistic process environments
- Membrane, Systems, and Economic Analyses

Membrane Fabrication

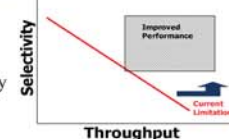
- Ultrasonic (US) atomization based deposition enables repeatable membrane fabrication in planar and tubular formats
- US produces low velocity, homogeneous droplets with precise and controllable liquid delivery rates for ultra-thin film deposition.



- High operating temperature (up to 150 °C)
- In-situ film processing capability
- Fully computer controlled via LabView
- Controlled coating environment

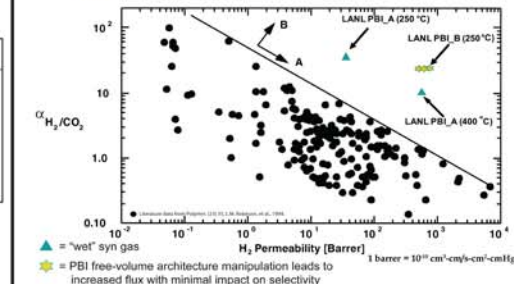
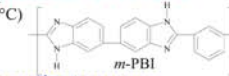
High T Polymeric Membranes

- Commercially available polymer membranes are limited to 150 °C operating temperature
 - Economic advantages of membrane separations are strongly tied to process/separation temperature
- Tradeoff between selectivity and productivity has proven difficult to overcome
- Chemical & mechanical stability and durability are often elusive
 - Commercial viability driven by combination



PBI-Based Thermoplastics: Overview

- Thermally stable ($T_g \sim 450 - 500^\circ\text{C}$)
- Mechanically and chemically robust
 - Sulfur and carbon tolerance at operating temperatures
- Processable - Standalone films, hollow fibers and thin films on porous substrates
- Excellent combination of permeability and selectivity
 - Well above the Robeson upper bound for polymeric membranes at process relevant temperatures

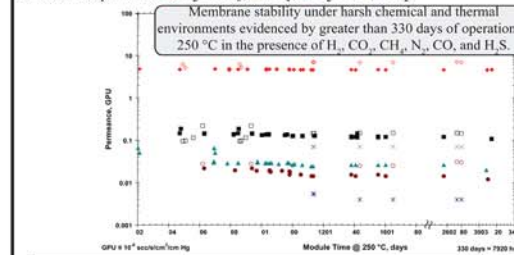


▲ = "wet" syn gas
★ = PBI free-volume architecture manipulation leads to increased flux with minimal impact on selectivity

Durability

Single Gas Experiments: \diamond H₂, \blacksquare CO₂, \blacktriangle CH₄, \triangle N₂

Mixed Gas Experiments: \diamond H₂, \square CO₂, \square CH₄, \triangle N₂, \times H₂S



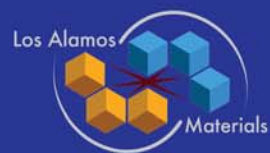
NETL Acknowledgements

The presented project work supports the U.S. DOE Energy Efficiency and Renewable Energy Industrial Technologies Program and the U.S. DOE Office of Fossil Energy - National Energy Technology Sequestration Program. The authors gratefully acknowledge the U.S. DOE/EERE-ITP and the U.S. DOE NETL Sequestration Program for financial support of the projects under contracts LANL CPS #18990 and FWP FE-10-002/ DE-FC26-07NE43090.



Project Partners





Chemical H₂ storage research at LANL

A. Burrell, B. Davis, H. Diyalanage, MPA-MC; J. Gordon, C-IIAC; T. Nakagawa, MPA-MC;
K. Ott, SPO-AE; T. Semelsberger, R. Shrestha, MPA-MC; F. Stephens, A. Sutton, C-IIAC



Chemical Hydrogen Storage Center of Excellence (CHSCoE)

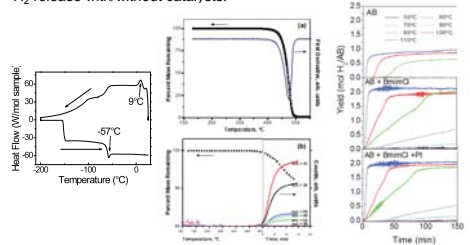
CHSCoE was a collaboration of academic, industrial, and national labs utilizing fundamental & applied approaches, along with a rapid down-select criteria, to evolve H₂ storage technology. LANL co-lead the center with PNNL from 2005-2010.

H₂ Release

LANL continues work on ammonia borane (AB, H₃NBH₃, 19.6 wt % H₂), a stable solid with exothermic H₂ release. Engineering concerns intensify LANL focus on fluid phase AB.

Argonne analysis showed ~11 wt. % AB/ionic liquid (IL) can lead to a workable system of 4.8% (ultimate DOE target = 7.5%).

In collaboration with Penn, ionic liquids were screened for suitability, including low temperature DSC, TGA decomposition, and thermolytic H₂ release with/without catalysts.



Initial long term stability testing of AB in ILs show no degradation at 50 °C; however, the total AB loadings are insufficient to meet DOE metrics. Future work is focused on binary and ternary IL combinations to enhance solubility, pre- and post-H₂ release.

Spent Fuel Regeneration

- Single reagent discovered, hydrazine
- Works on multiple forms of spent fuel
- Demonstrated in ionic liquids
- Completed assessment of hydrazine regeneration with DOW chemical
- Inefficient hydrazine synthesis is the culprit; contributes to 95% of cost
- Now there are two efficient methods of AB regeneration, none in 2007

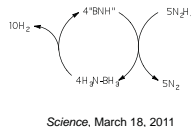
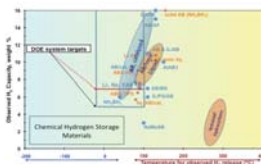


Table 1. AB Regeneration Test Results (AB: Spent Fuel Regeneration)

Run	AB (g)	Regeneration (g)	Regeneration (%)
1	1.0	0.8	80
2	1.0	0.8	80
3	1.0	0.8	80
4	1.0	0.8	80
5	1.0	0.8	80
6	1.0	0.8	80
7	1.0	0.8	80
8	1.0	0.8	80
9	1.0	0.8	80
10	1.0	0.8	80

Challenges

- Materials without phase change upon dehydrogenation
- Maximizing AB in IL while being stable
- Efficient hydrazine synthesis or new regeneration methodology



Materials
Status

Summary

- CHSCoE narrowed focus to fluid phase H₂ storage materials, impurity quantification, regeneration assessments
- ECoE built/tested small scale test bed for controlled H₂ release, mitigated impurities, and demonstrated an acoustic fuel gauge



Collaborations



Collaborations

Engineering Center of Excellence (ECoE)

Started in 2009, the ECoE is charged with vehicular system design for hydrogen storage materials which meet DOE target. LANL has several tasks as part of the ECoE, including fluid phase system design, rate modeling, fuel gauge development, and impurity measurement/mitigation.

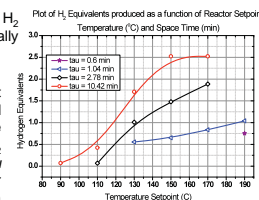
Fluid Phase Validation Test Bed

To evaluate thermolytic H₂ release and impurities from fluid phase H₂ storage materials, a validation test bed was constructed and initially operated with 5% AB in tetraglyme.



Validation Test Bed

H₂ release was measured at different flow rates and temperatures, to determine optimal contact time; the H₂ stream can be analyzed *in-situ* with FTIR and microGC for impurities. Scrubbing media can be as well.



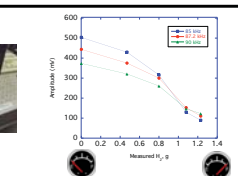
5% AB in Tetraglyme

Acoustic Fuel Gauge Sensor

A non-invasive sensor has been designed to measure the state of H₂ loading in metal hydride containing fuel tanks (patent filed). Proof of concept studies are complete; cycling work has begun. Future work includes evaluation of chemical hydride tanks and cryogenic adsorption tanks.

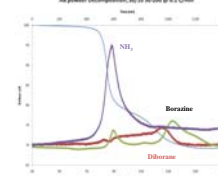


Test Tank



Impurity Measurement and Mitigation

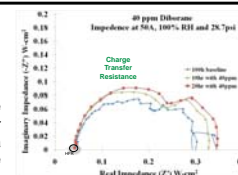
Small impurities may degrade fuel cell performance over time, so identification, quantification, and mitigation are essential.



NH₃, borazine, and diborane have been quantified by FTIR for solid AB. Adsorption media successfully scrubs these species. Future work will focus on fluid phase compositions.

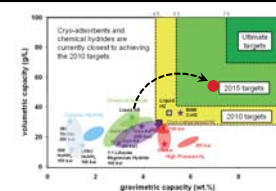
Adsorption Media Tested

1. Ammonia sorbent II
2. Selexsorb CD
3. Carbon
4. Zeolites + others



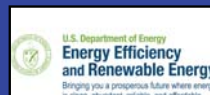
Fuel cell tolerance tests are used to bound acceptable levels. The diborane immediately reacts with the humid air, hence borates are responsible for the charge transfer resistance.

System
Status



Challenges

- Validating system-level modeling assumptions
- Validate novel component designs for performance and viability
- Materials development





Ions to Wires: The Science of High- T_c Superconducting Wires

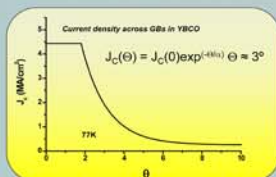
T. G. Holesinger, B. Maiorov, L. Civale, S.P. Ashworth, V. Matias, J.R. Groves, D.N. Nguyen, Q.X. Jia, J.L. Driscoll, I. Usov, R.F. DePaula, J.Y. Coulter, P.C. Dowden, J. Kennison, C. Sheehan, J. Rowley, D.E. Peterson (ret.), S.R. Foltyn (ret.), P.A. Arendt (ret.), J.O. Willis, K.R. Marken (Group Leader)
MPA-STC

Overview

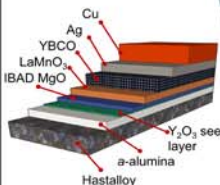
LANL has pioneered the development of the coated conductors – high-temperature superconducting (HTS) wires – which permit dramatically greater current densities than conventional copper cable, and enable new technologies to secure the national power grid. Sustained world-class research from concept, extreme performance demonstration, transfer, and ongoing industry support has moved this idea from the laboratory to the commercial marketplace.

Problem

$Y_1Ba_2Cu_3O_7$ (YBCO), is a brittle ceramic with stringent demands for bi-axial alignment to support high critical current (I_c) transport.



LANL Solution

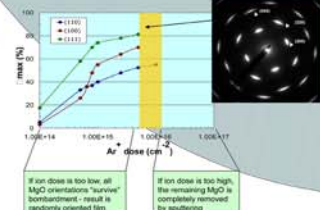
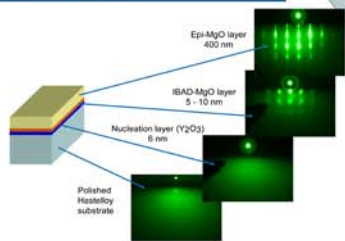
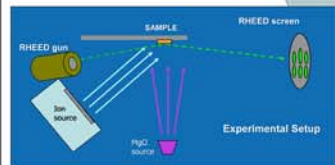


Flexible, robust wire based on YBCO deposition on film-textured surfaces on polycrystalline superalloy tapes. LANL patented Ion-Beam Assisted Deposition (IBAD) technology allows for near single-crystal quality oxide layers of MgO may produced in arbitrary lengths (> 1 km!).

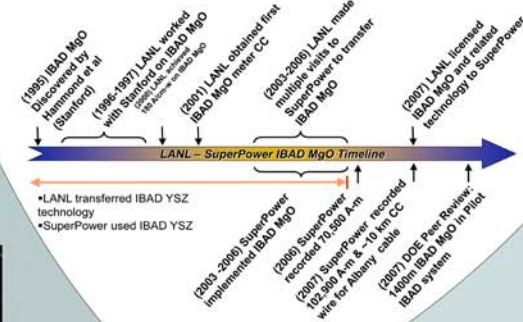
Demonstration

The first continuously processed meter length tape initiated industry adoption of technology (1998)

Flexible Superconducting Tape



Energy Security through World Class Science



Technology Transfer

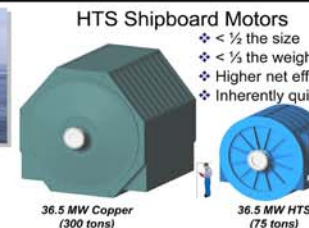
Science Underpinning the Technology: (selected references)

X.D. Wu et al, *App. Phys. Lett.*, **65** pp. 1961-1963 (1994)
J.L. MacManus-Driscoll et al, *Nature Materials*, **3** pp. 439-443 (2004)
Foltyn et al, *Nature Materials*, **6** pp. 631-642 (2007)
L. Civale et al, *App. Phys. Lett.*, **84** pp. 2121-2123 (2004)
Feldmann et al, *App. Phys. Lett.*, **91** 162501 (2007)
Feldmann et al, *Supercond Sci. Technol.*, **23** 115016 (2010)

Arendt et al, *MRS Bulletin*, **29** pp. 543-550 (2004)
Maiorov et al, *Nature Materials*, **8** pp. 398-404 (2009)
Holesinger et al, *Advanced Materials*, **20** pp. 391-407 (2008)
Holesinger et al, *Supercond Sci. Technol.*, **22** 04025 (2009)
Matias et al, *Supercond Sci. Technol.*, **23** 014018 (2010)
Feldmann et al, *Supercond Sci. Technol.*, **23** 095004 (2010)



Navy All-Electric Ship



HTS Shipboard Motors

- < 1/2 the size
- < 1/2 the weight
- Higher net efficiency
- Inherently quieter



Long Island Cable Project
... 600 MW and transmission voltage of 138 kV... carry enough power to serve 300,000 homes...

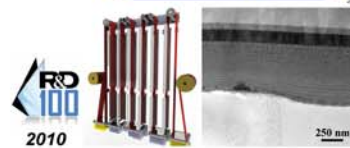


Wind Turbines
Direct Drive – no gear box.
High Efficiency
Enabling 10MW + turbines for off-shore wind farms

Application Development

MPA-STC works with industry to design new electric power applications of HTS wire, build prototype devices, and engineer conductor designs to minimize AC losses.

Wire Characterization



Solution Deposition Planarization (SDP)

Process Development



In-line $I_c(\theta)$ measurements

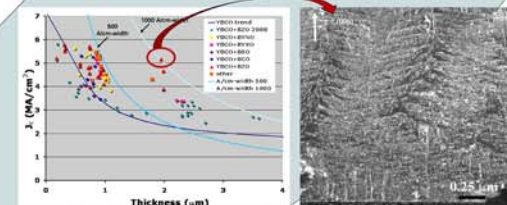
Industry Support

Materials development, electromagnetic, and structural characterization in support of industry's HTS wire efforts results in reliable manufacturing and performance enhancing technologies. An example of sustained industry support is the LANL-American Superconductor CRADA which is entering its 23rd year.

Extreme Performance

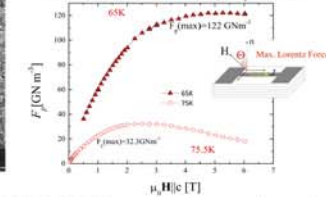
LANL materials development efforts identified pathways to record performance in thick YBCO films.

World record self-field J_c (5 MA/cm² = 2 μm) in YBCO thick films with BaZrO₃ nanorods and Y₂O₃ nanoparticle layers.

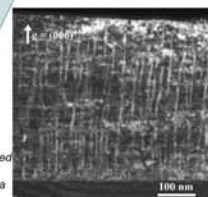


Structure-Property-Chemistry Relationships

World record flux pinning force (122 GNm⁻², 65 K) in films with self-assembled YBa₂NbO₆ nanorods.



Materials Development



Self-assembled YBa₂NbO₆ nanorods in a YBCO film.



Sustainability: The High T_c program has been a resounding success in LANL's portfolio of energy security research. Its success was enabled by the world-class talent it attracts and the sustained commitment to research from concept through commercialization and beyond. The high T_c program continues to address national needs through support of the fledgling HTS industry.